Please provide feedback

Please support the ScholarWorks@UMBC repository by emailing scholarworks-group@umbc.edu and telling us what having access to this work means to you and why it's important to you. Thank you.

The Streamer Blowout Origin of a Flux Rope and Energetic Particle Event Observed by Parker Solar Probe at 0.5 au

D. Lario[1] ✪, L. Balmaceda[1,2] ✪, N. Alzate[1,3] ✪, M. L. Mays[1], I. G. Richardson[1,4] ✪, R. C. Allen[5] ✪, M. Florido-Llinas[6],
T. Nieves-Chinchilla[1] ✪, A. Koval[1,7], N. Lugaz[8] ✪, L. K. Jian[1] ✪, C. N. Arge[1], P. J. Macneice[1], D. Odstrcil[1,2], H. Morgan[9],
A. Szabo[1], M. I. Desai[10,11] ✪, P. L. Whittlesey[12] ✪, M. L. Stevens[13], G. C. Ho[5], and J. G. Luhmann[12] ✪

[1] NASA, Goddard Space Flight Center, Heliophysics Science Division, Greenbelt, MD 20771, USA; david.larioloyo@nasa.gov
[2] George Mason University, Fairfax, VA 22030, USA
[3] Universities Space Research Association (USRA). Columbia, MD 21046, USA
[4] University of Maryland, Department of Astronomy, College Park, MD 20742, USA
[5] The Johns Hopkins University, Applied Physics Laboratory, Laurel MD 20723, USA
[6] Interdisciplinary Higher Education Center (CFIS) Universitat Politècnica de Catalunya, Barcelona E-08028, Spain
[7] Goddard Planetary Heliophysics Institute, University of Maryland, Baltimore County, Baltimore, MD 21250, USA
[8] Institute for the Study of Earth, Oceans, and Space, Department of Physics, University of New Hampshire, Durham, NH 03824, USA
[9] Department of Physics, Prifysgol Aberystwyth, Aberystwyth, Cymru SY23 3BZ, UK
[10] Department of Physics and Astronomy, University of Texas at San Antonio, San Antonio, TX 78249, USA
[11] Southwest Research Institute, San Antonio, TX 78249, USA
[12] Space Science Laboratory, University of California, Berkeley, CA 94720, USA
[13] Center for Astrophysics—Harvard & Smithsonian, MA, USA

Abstract

The distribution of spacecraft in the inner heliosphere during 2019 March enabled comprehensive observations of an interplanetary coronal mass ejection (ICME) that encountered Parker Solar Probe (PSP) at 0.547 au from the Sun. This ICME originated as a slow ($\sim$311 km s^{-1}) streamer blowout (SBO) on the Sun as measured by the white-light coronagraphs on board the Solar TErrestrial RElations Observatory-A and the Solar and Heliospheric Observatory. Despite its low initial speed, the passage of the ICME at PSP was preceded by an anisotropic, energetic ($\lesssim$100 keV/n) ion enhancement and by two interplanetary shocks. The ICME was embedded between slow ($\sim$300 km s^{-1}) solar wind and a following, relatively high-speed ($\sim$500 km s^{-1}), stream that most likely was responsible for the unexpectedly short (based on the SBO speed) ICME transit time of less than $\sim$56 hr between the Sun and PSP, and for the formation of the preceding shocks. By assuming a graduated cylindrical shell (GCS) model for the SBO that expands self-similarly with time, we estimate the propagation direction and morphology of the SBO near the Sun. We reconstruct the flux-rope structure of the in situ ICME assuming an elliptic-cylindrical topology and compare it with the portion of the 3D flux-rope GCS morphology intercepted by PSP. ADAPT-WSA-ENLIL-Cone magnetohydrodynamic simulations are used to illustrate the ICME propagation in a structured background solar wind and estimate the time when PSP established magnetic connection with the compressed region that formed in front of the ICME. This time is consistent with the arrival at PSP of energetic particles accelerated upstream of the ICME.

Unified Astronomy Thesaurus concepts: Solar coronal mass ejections (310); Ejecta (453); Solar energetic particles (1491); Interplanetary particle acceleration (826); Solar coronal mass ejection shocks (1997)

Supporting material: animations

1. Introduction

Streamer blowouts (SBOs) are a particular class of coronal mass ejections (CMEs) characterized by a gradual swelling of the overlying coronal streamer followed by a usually well-structured, but generally slow, CME that emerges from the streamer belt (Sheeley et al. 1982; Illing & Hundhausen 1984). SBO-CMEs originate in extended polarity inversion lines outside of active regions, and their average duration, from the start of the streamer swelling to the release of the CME, is about 40.5 hr (Vourlidas & Webb 2018). The fact that SBO-CMEs usually lack strong solar surface signatures as seen in extreme-ultraviolet (EUV) or other solar surface measurements (e.g., Nitta & Mulligan 2017, and references therein) fits with the model of "stealth" CMEs proposed by Lynch et al. (2016). In this model, the pre-eruptive magnetic field configuration of an SBO-CME is that of a sheared arcade energized via photospheric shearing motions within a multipolar field configuration. The shearing motions lead to magnetic reconnection within the sheared arcade, which slowly

expands and transitions into an erupting flux rope that gradually accelerates as it moves outward. The result is a slow SBO-CME that originates in closed field regions at a certain height above the solar photosphere with a spatial extent that is larger than those of streamer blobs but much less energetic than fast CMEs (Lynch et al. 2016). Therefore, the mechanism of SBO-CMEs (i.e., release of magnetic energy accumulated by differential rotation) is not intrinsically different from flare-related CMEs, except for the higher altitude where the reconnection takes place and the smaller amounts of magnetic energy available (Vourlidas & Webb 2018). In fact, the in situ signatures of the passage of an SBO-CME over a spacecraft do not differ significantly from those typical of interplanetary CMEs (ICMEs) associated with flare-related CMEs (e.g., Lynch et al. 2010), including a smooth magnetic field with slow rotation, low plasma β, and bidirectional suprathermal electrons (BDEs; e.g., Zurbuchen & Richardson 2006, and references therein). In this article we will use the term CME or SBO-CME for those structures usually observed in

coronagraph images and ICME for the related structures propagating in interplanetary (IP) space.

The slow evolution of SBO-CMEs casts some doubts about their ability to drive shocks capable of energetic particle acceleration. During its first orbit around the Sun, in situ instruments on board the Parker Solar Probe (PSP) detected an ICME at 0.25 au (54.7 $R_\odot$) from the Sun (Korreck et al. 2020; Nieves-Chinchilla et al. 2020). The ICME, observed by PSP on 2018 November 11 at 0.25 au, originated as a slow SBO-CME on the Sun initially moving at $\sim$249 km s^{-1} (speed estimated between 6 and 14 $R_\odot$ from the center of the Sun; Korreck et al. 2020). The average transit speed of the nose of this SBO-CME when traveling from $\sim$6 $R_\odot$ (on 2018 November 10 at 22:30 UT) to its arrival at PSP at 54.7 $R_\odot$ (on 2018 November 11 at 23:53 UT) was about $\sim$370 km s^{-1} (Korreck et al. 2020), implying that at some point during its trajectory the CME accelerated (Nieves-Chinchilla et al. 2020). One distinct in situ signature of this ICME at PSP was the absence of a preceding shock. Nevertheless, a significant low-energy ($\lesssim$200 keV/n) ion intensity enhancement was observed by PSP. Giacalone et al. (2020) interpreted this energetic particle increase as a consequence of particle acceleration occurring either at plasma compressions formed in front of the propagating ICME or at a weak shock initially driven by the CME that was not detected at its arrival at PSP. The source of these particles could only accelerate ions up to a few hundred keV and was inferred to turn on at a heliocentric distance of $\sim$7.4 $R_\odot$ and co-move with the ICME. The injection of particles from this moving source lasted only a few hours, depending on the ion energy, and had ceased before its arrival at PSP (see details in Giacalone et al. 2020). An alternative scenario explaining the origin of the energetic particle enhancement associated with this SBO-CME can be found in Mitchell et al. (2020).

The propagation of an ICME through the inner heliosphere depends not only on the initial speed of the parent CME but also on the ambient solar wind medium through which it propagates (e.g., Case et al. 2008). When a CME starts interacting with the ambient solar wind, its bulk speed tends to approach that of the ambient solar wind (Gopalswamy et al. 2000). The evolution of the bulk speed of a typical slow CME can be approximately described by two phases: a gradual acceleration out to about $\sim$20–30 $R_\odot$, followed by a near constant speed similar to that of the ambient solar wind (Liu et al. 2016). Additionally, during their propagation through IP space, ICMEs might also expand. A slow ICME moving through a high-speed solar wind stream (HSS) tends to expand quickly due to the tenuous fast ambient plasma, reducing the transit time and resulting in a smaller density jump (Δn) and larger velocity jump (ΔV) observed before ICME arrival than would have occurred if the ICME were propagating through slower denser solar wind (Pizzo et al. 2015). For an ICME propagating through a structured solar wind formed by streams of different speeds, the ICME, or portions of it, may be accelerated or decelerated, resulting in distortions of the ICME that depend on the configuration of the streams and their relationship to the CME launch site (e.g., Pizzo et al. 2015; Liu et al. 2016, 2019). Slower ICMEs also have relatively more time to interact with other solar wind structures as they move away from the Sun. Cases have been frequently observed of ICMEs that are deformed and slowly accelerated by the pressure exerted by a following HSS (e.g., Liu et al. 2016) or compressed when entrained between slow and fast solar wind

streams (e.g., Rouillard et al. 2009; He et al. 2018; Heinemann et al. 2019).

In this article, we analyze an ICME observed by PSP during its second orbit around the Sun at a heliocentric radial distance $R = 0.547$ au. This ICME displayed properties of a magnetic cloud (MC) and was followed by a fast solar wind stream (Section 2). The origin of this ICME was found to be an SBO-CME that was slowly released from the Sun $\sim$56 hr earlier (Section 3). In Section 4, we analyze the evolution of the ICME in IP space. It is inferred that the leading edge of a corotating HSS emanating from an equatorial extension of the southern coronal hole (CH) close to the launch site of the CME compressed the MC on its way to PSP (Section 4.1). The arrival of the ICME was accompanied by a preceding low-energy ($\lesssim$100 keV/n) particle event. Magnetohydrodynamic (MHD) simulations are used to describe the propagation of the ICME in IP space and its arrival at PSP and to determine when magnetic connection was established between PSP and the shocks potentially driven by the ICME. This is consistent with the time of arrival of energetic particles at PSP, and hence that these particles were most likely accelerated by the compressions that formed in front of the ICME (Section 4.2). Finally, Sections 5 and 6 discuss and summarize, respectively, the main results of the study.

2. In Situ Measurements

In situ measurements of plasma, magnetic field, and energetic particles at PSP presented in this paper were collected by the Solar Wind Electrons Alphas and Protons (SWEAP; Kasper et al. 2016), the FIELDS (Bale et al. 2016), and the Integrated Science Investigation of the Sun (IS⊙IS; McComas et al. 2016) instrument suites, respectively. The SWEAP instrument suite consists of the Solar Probe Cup (SPC), which measures the solar wind proton temperature, density, and velocity (Case et al. 2020), and two Solar Probe Analyzers (SPANs) capable of measuring solar wind electrons on the ram (ahead) and anti-ram (behind) faces of the spacecraft (SPAN-A-E and SPAN-B-E), which together measure the majority of the 3D electron velocity distribution function (Whittlesey et al. 2020). The FIELDS experiment includes two fluxgate magnetometers and a search-coil (induction) magnetometer mounted on a deployable boom in the spacecraft umbra that allows for clean measurements of the interplanetary magnetic field (IMF). The IS⊙IS consists of a suite of two energetic particle instruments: (1) EPI-Lo, which measures particles using the time-of-flight (ToF) versus energy technique and determines the composition, spectra, and anisotropies of particles with energies from $\sim$20 keV nucleon^{-1} to several MeV nucleon^{-1} (Hill et al. 2017), and (2) EPI-Hi, which uses the dE/dx versus residual energy technique to measure particles over the energy range of $\sim$1–200 MeV nucleon^{-1} (Wiedenbeck et al. 2017).

Figure 1 displays a subset of these measurements made from 2019 March 13 at 00:00 UT to 2019 March 16 at 12:00 UT. From top to bottom, Figure 1 shows the (a) radial V_R, (b) tangential V_T, and (c) normal V_N components of the solar wind proton velocity in the spacecraft-centered Radial–Tangential–Normal (RTN) coordinate system, as well as (d) solar wind proton density N_p, and (e) solar wind proton temperature T_p as measured by SWEAP/SPC. Panel (f) shows the magnetic field magnitude B, (g) shows the elevation angle θ_{IMF}, and (h) shows the azimuthal angle ϕ_{IMF} of the magnetic field vector $\boldsymbol{B}$ in RTN
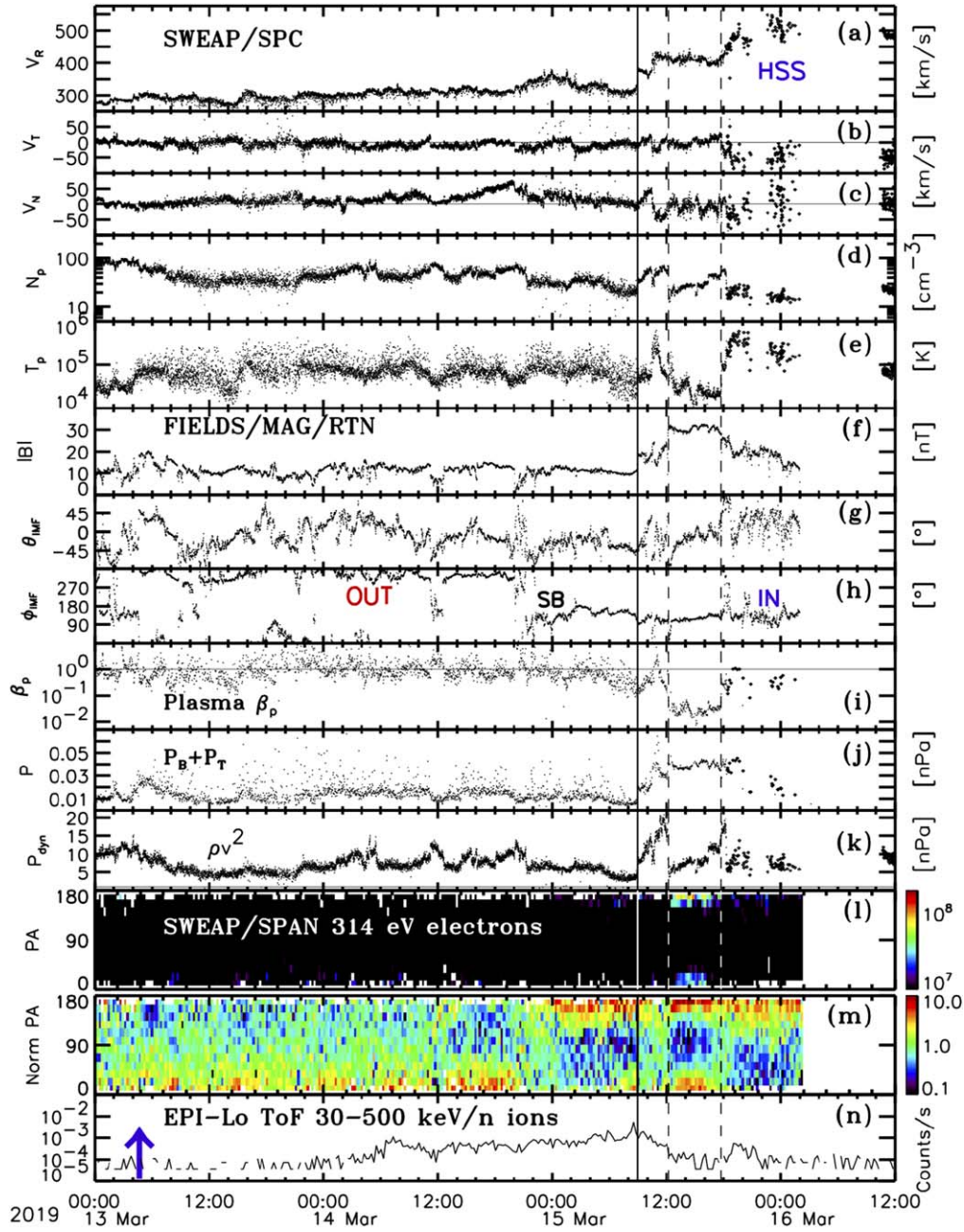
Figure 1. From top to bottom, (a) radial V_R, (b) tangential V_T, and (c) normal V_N components of the solar wind proton velocity in the PSP centered RTN coordinated system, (d) solar wind proton density N_p, and (e) solar wind proton temperature T_p as measured by SWEAP/SPC; magnetic field (f) magnitude B, (g) elevation and (h) azimuth angles in the spacecraft-centered RTN coordinate system as measured by FIELDS; (i) proton plasma beta β_p; (j) the sum of the magnetic pressure P_B and thermal pressure P_T; (k) ram pressure P_{dyn}; (l) 314 eV electron pitch-angle (PA) distributions, and (m) 314 eV electron normalized PADs as measured by SWEAP/SPAN; and (n) low-energy (∼30–500 keV) ion intensities measured by the ToF system of EPI-Lo. The vertical solid line indicates the passage of two IP shocks that are too close in time to resolve here (see Section 2.2). The vertical dashed lines indicate the arrival and departure times of the ICME. The vertical blue arrow in panel (n) indicates the time when the parent SBO eruption on the Sun accelerated (see Section 3).

coordinates as measured by PSP/FIELDS. Panel (i) shows the proton β parameter computed as $\beta_p = N_p \kappa T_p / (B^2/8\pi)$, and (j) shows the pressure P given by the sum of the magnetic field pressure $P_B = B^2/8\pi$ and an approximation of the thermal plasma pressure computed as $P_T = 2.24(N_p \kappa T_p)$, which estimates the proton, electron, and heavy ion contributions to the plasma thermal pressure. Panel (k) shows the dynamic pressure computed as $P_{dyn} = N_p V_R^2$. Panel (l) shows the 314 eV electron raw fluxes as a function of pitch angle as measured by the combination of SPAN-A-E and SPAN-B-E in units of e/(s sr cm² eV). Panel (m) shows the 314 eV electron

pitch-angle distributions (PADs) normalized to the mean flux over all pitch angles at each data point. Panel (n) shows the flux of energetic ions at energies between ∼30 and ∼500 keV/n as measured by the ToF system of EPI-Lo.

The two dashed vertical lines in Figure 1 indicate the passage of an ICME from ∼12:14 UT to ∼17:45 UT on 2019 March 15. Signatures typical of an ICME (e.g., Zurbuchen & Richardson 2006) are easily identifiable in Figure 1, including: depressed T_p, low β_p, enhanced magnetic field magnitude with a gradual change in the field direction also characteristic of an MC (Klein & Burlaga 1982), the presence of field-aligned
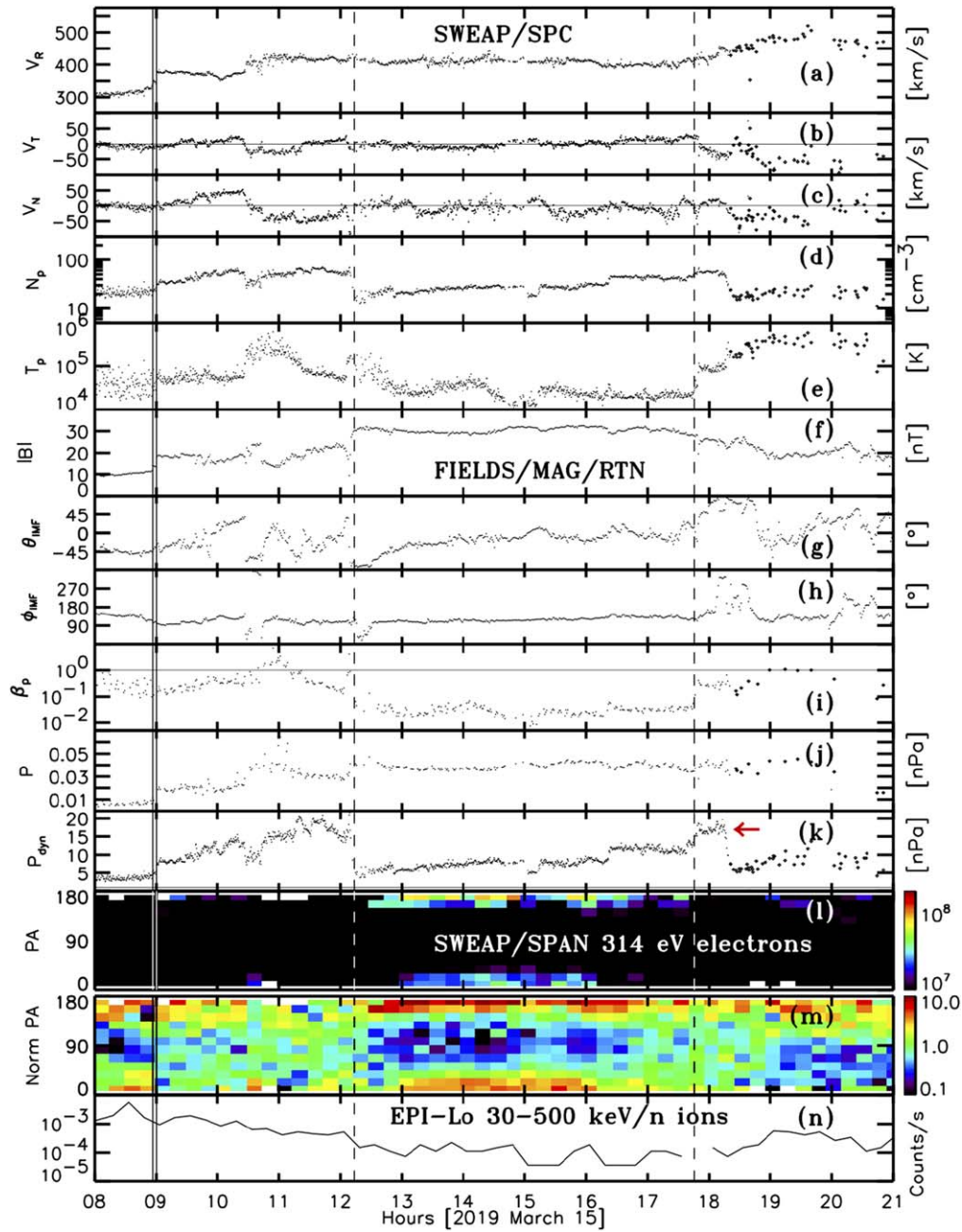
Figure 2. The same as Figure 1 but for the time interval 08:00 UT to 21:00 UT on 2019 March 15. The two vertical solid lines indicate the passage of two IP shocks (see Section 2.2).

BDEs, indicated by the enhancements at $0°$ and $180°$ in Figures 1(l) and (m), suggesting that this structure contained looped field lines rooted at the Sun at both ends (e.g., Gosling 1990), and also the decrease of energetic particle intensities with respect to those observed immediately before and after its passage (Figure 1(n)).

Figure 2 zooms in around the time interval of the ICME passage. The ICME boundaries are well defined by the near simultaneous discontinuities of β_p, $P_{\rm dyn}$, B, and $\theta_{\rm IMF}$ at its leading and trailing edges. The ICME was preceded by two IP shocks at 08:56:01 UT and 09:00:07 UT, indicated by the solid vertical lines in Figure 2, which will be discussed further in Section 2.2. A sheath region characterized by compressed plasma with enhanced V_R, N_p, and hence a large $P_{\rm dyn}$, with oscillating magnetic field $\theta_{\rm IMF}$ orientations, as well as

deflections in the solar wind V_T and V_N speed components, was observed for a period of ~ 3.25 hr between the shocks and the leading edge of the ICME. The duration of this sheath region (~ 3.25 hr) is within the range of sheath durations observed by the MErcury Surface, Space ENvironment, GEochemistry, and Ranging (MESSENGER) mission at distances $0.309 < R < 0.463$ au (that had an average duration of ~ 2.4 hr), but contrasts with the average sheath duration at 1 au of about ~ 12 hr (Janvier et al. 2019). The thickness of an ICME sheath depends on both (i) how much plasma from the corona and upstream solar wind is accreted, compressed, and piled up in front of the ICME, and (ii) how much of it is able to escape toward the sides of the main body of the ICME (Siscoe & Odstrcil 2008). The expansion of a sheath with heliocentric distance has been interpreted as a result of the progressive

accretion of overtaken plasma in front of the ICME that increases as the ICME propagates outward (DeForest et al. 2013; Janvier et al. 2019).

The duration Δt of the ICME passage by PSP was only ~5.52 hr. By assuming a linear increase of Δt with heliocentric distance, the duration of this ICME at 1 au would have been of ~10 hr. This duration puts this ICME in the low end of the distribution of ICME durations at 1 au (e.g., Nieves-Chinchilla et al. 2018b), even at solar minimum (see Figure 17 in Jian et al. 2018), and in the upper end of the distribution of small-scale flux-rope transits at 1 au (as per the definition of small-scale flux ropes used by Cartwright & Moldwin 2008, 2010a). Note that other dependences to extrapolate the ICME duration with radial distance would have resulted in shorter durations at 1 au (for example, ~7 hr in the case of an $R^{0.37}$ dependence inferred for small-scale flux ropes by Cartwright & Moldwin 2010b). The average duration of the ICMEs observed by MESSENGER at ~0.4 au was 7.2 hr, with a ratio between the sheath and the ICME durations of 0.33 (Janvier et al. 2019). Figure 2 shows that for the ICME at PSP, this ratio was 0.59, suggesting that the duration of the ICME was relatively short compared to the sheath duration.

The fall in V_R between the leading and trailing edge of the ICME has been usually interpreted as a measure of its expansion rate, but for this ICME, it was only $\Delta V_R \sim 6 \, \text{km s}^{-1}$, with a slope measured during its passage of only $dV_R/dt \sim 0.3 \, \text{m s}^{-2}$. The average solar wind speed in the ICME was ~407 km s^{-1}. The expansion of MCs in the radial direction has been characterized by the nondimensional parameter ζ defined by Gulisano et al. (2010, 2012) as $\frac{dV_R}{dt} \frac{D}{V_c^2}$, where D is the heliocentric radial distance where the MC is observed, and V_c is the velocity at the center of the MC. For the specific MC at PSP, we obtain $\zeta \sim 0.15$, which is comparatively smaller than the typical value observed in MCs propagating between 0.3 and 1.0 au under unperturbed solar wind conditions (i.e., 0.91 ± 0.23; Gulisano et al. 2010). Using MCs for which their propagation was considered to be perturbed by the solar wind environment, Gulisano et al. (2010) inferred a large variability in the values of ζ with a smaller average value of 0.48 ± 0.79. Therefore, the in situ measurements indicate that the MC observed by PSP at $R = 0.547$ au was a very slowly expanding ICME and may have been significantly perturbed by the ambient solar wind.

The trailing edge of the ICME was followed by a relatively fast (~500 km s^{-1}), hot ($T_p \gtrsim 10^5$ K), and tenuous (~10 cm^{-3}) solar wind stream that we label HSS in Figure 1. On the other hand, the solar wind was slow (~300 km s^{-1}) ahead of the shocks, indicating that the ICME was bracketed between slow and fast solar wind streams, a configuration that presumably influenced its propagation. In particular, the brief increase in P_{dyn} immediately following the ICME (indicated by a red arrow in Figure 2(k)) is possible evidence of the following HSS exerting pressure on the ICME. The low value of ζ might also be evidence that the ICME expansion is perturbed by the ambient solar wind. Another signature of the interaction between the HSS and ICME may be the deflection of the solar wind flow toward the east, evident as an increase in the negative V_T component in Figure 2(b) between the trailing edge of the ICME and the leading part of the HSS. Such eastward deflections also occur in corotating interaction regions (CIRs) in the decelerated fast solar wind following the stream interface due to the interaction with the slow solar wind ahead of the interface (Richardson 2018). A corresponding deflection to the west usually occurs in the slow solar wind ahead of

the interface, but is not observed in Figure 1 because of the presence of the ICME. Thus, the transverse deflection of the HSS leading edge suggests that it is similarly interacting with the preceding ICME. Deflections of the solar wind velocity in the compressed sheath in front of the ICME, evident in V_T and V_N, are most likely a consequence of the plasma draping around the ICME and a signature of the interaction between the ICME (driven by the HSS) and the upstream solar wind. In addition, upstream of the shocks, the prominent increase in V_N around ~20:00 UT on March 14 (Figure 1(c)) is in close proximity to the heliospheric current sheet (HCS) as evidenced by the magnetic field sector boundary changing from outward to inward polarity (indicated by SB in Figure 1(h)) and by the corresponding reversal in the suprathermal electron pitch angle distribution in Figure 1(m).

Figure 2(n) shows that energetic particle intensities maximized ~23 minutes before the arrival of the shocks. This might have occurred if, before the shock crossings, PSP was magnetically connected to remote regions of the shocks where particle acceleration was more efficient than where the spacecraft crossed the shocks. It is interesting to note the presence of suprathermal electron PADs indicative of BDEs or loss-cone distributions during this time interval prior to the arrival of the shocks (between ~08:15 UT and ~09:00 UT in Figures 1(m) and 2(m)). These PADs might be a consequence of magnetic connection with remote portions of the shock surface caused by ripples able to reflect suprathermal electrons that are sampled by the spacecraft just before the arrival of the shocks (e.g., Feldman et al. 1983; Pulupa & Bale 2008). BDEs were more prominent during the passage of the ICME, starting at ~13:00 UT just inside the leading edge, and declined from ~16:10 UT to the trailing edge (Figure 2(m)). The presence of weaker BDEs near the edges of ICMEs has also been frequently observed at 1 au and has been interpreted as evidence for a mixture of open field lines, resulting from the reconnection of formerly closed field lines with the ambient IMF, and closed field lines (e.g., Carcaboso et al. 2020, and references therein). Additionally, there is a certain imbalance in the BDE flows in the ICME with a larger flux at pitch angles ~180° corresponding, with an inward magnetic field, to electrons flowing away from the Sun. Such an imbalance can occur when the observing spacecraft is closer to one flux-rope footpoint as discussed by, for example, Pilipp et al. (1987), Phillips et al. (1992), and Kahler et al. (1999). On the other hand, suprathermal electron PADs were more isotropic in the sheath and post-ICME intervals, which could result from enhanced scattering conditions and the reflection of electrons in converging lines around the ICME and/or at the two shocks (Carcaboso et al. 2020).

2.1. MC In Situ 3D Reconstruction

The PSP in situ observations allow us to estimate the orientation and size of the MC. We have applied the circular-cylindrical (CC) and elliptical-cylindrical (EC) analytical models, described by Nieves-Chinchilla et al. (2016, 2018a) to infer the morphology and orientation of the MC. The CC model is a generalization of the CC concept of Hidalgo et al. (2002) in terms of the radial dependence of the poloidal current density component and the axial current density component. This generalization provides the flexibility to explore the internal forces that dominate flux-rope evolution, in addition to providing the usual parameters that define the flux-rope

Model	C_{10}	B_0^y (nT)	Φ (deg)	Θ (deg)	ξ (deg)	y_0 (au)	δ	r (au)	ϕ_y (10^{21} Mx)	ϕ_φ (10^8 Mx m^{-1})	χ^2
(1)	(2)	(3)	(4)	(5)	(6)	(7)	(8)	(9)	(10)	(11)	(12)
CC	5.50	140.	173	−2.0	⋯	0.0077	1	0.0084	0.350	16.06	0.301
EC	2.48	74.8	169	−1.5	65	0.0103	0.83	0.0129	0.298	23.60	0.225

Note. Column (1) indicates the models used: CC and EC. Columns (2)–(8) are the fitting output parameters: (2) the force-freeness parameter, (3) the center magnetic field magnitude, (4–6) the longitude, latitude, and propagation tilt angle for a distorted cross section, (7) closest approach to the flux-rope center, and (8) distortion of the flux-rope cross section. Columns (9–11) are derived quantities: (9) the maximum cross-sectional radius, (10) the axial magnetic flux, and (11) the poloidal magnetic flux. Column (12) indicates the goodness of the fit. Descriptions of these parameters can be found in Nieves-Chinchilla et al. (2016, 2018a).
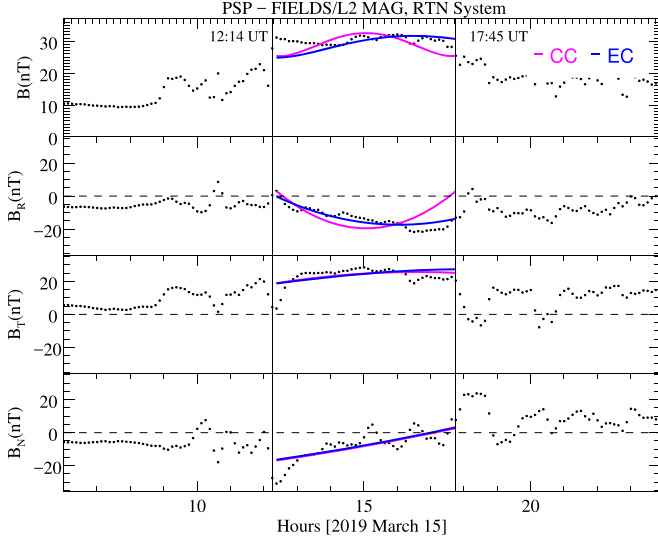

Figure 3. Comparison of the MC fitting results from the CC model (magenta) and the EC model (blue) with PSP magnetic field observations (from top to bottom, magnetic field magnitude B and the three components of **B** in the RTN coordinate system).

geometry and orientation. The EC model (Nieves-Chinchilla et al. 2018a) is based on the same physical principles but relaxes the geometrical constraint of the CC model and allows distortion of the flux-rope cross section. This model describes a cylindrical geometry with an elliptical cross section as the possible configuration for a distorted heliospheric flux rope. Thus, under this geometry, a flux rope is first described in a curved, non-orthogonal coordinate system. Both models allow us to directly compare the fitting results under similar assumptions.

Figure 3 shows the fitting results for both the CC (magenta) and EC (blue) models compared with the magnetic field measurements. With the exception of the enhanced magnetic field near the leading edge of the cloud, both models reproduce the magnetic field signatures, though the EC model better captures the field orientation near the trailing edge. The resulting fit parameters of both models are listed in Table 1. Both models agree that the orientation of the flux-rope axis (given in columns (4) and (5) by the longitude Φ and elevation Θ angles in the RTN coordinate system) was very closely aligned with the radial direction ($\Phi = 180°$) and nearly in the R–T plane ($\Theta = 0°$). Both models provide a very small radius r of the cross section of the MC as listed in column (9). The impact parameter y_0 (i.e., the closest approach distance of PSP to the flux-rope axis) is provided in column (7) indicating that,
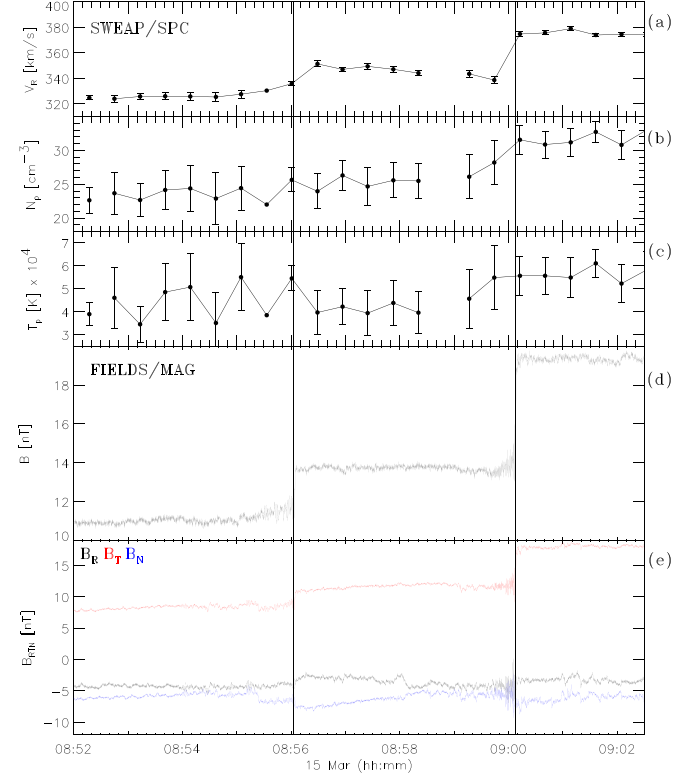

Figure 4. From top to bottom, (a) radial solar wind proton velocity V_R, (b) solar wind proton density N_p, and (c) solar wind proton temperature T_p as measured by SWEAP/SPC; (d) magnetic field magnitude B, and (e) magnetic field components in the spacecraft-centered RTN coordinate system as measured by FIELDS. The vertical solid lines indicate the passage of two IP shocks at 08:56:01 UT and 09:00:07 UT on 2019 March 15.

for both models, PSP intercepted the MC close to its edge, at a distance of ~90% (~80%) of its estimated cross-sectional radius from the axis of the flux rope, in the case of the CC (EC) model. The parameter δ provided in column (8) is the distortion of the flux-rope cross section ($\delta = 1$ for circular and $\delta \ll 1$ for highly elliptical). The EC model provides $\delta = 0.83$, suggesting a slight distortion with respect to a circular cross section.

2.2. Shock Properties

A peculiarity of this ICME was the observation of two closely spaced fast forward shocks preceding its arrival. Figure 4 shows, from top to bottom, V_R, N_p, and T_p as observed by PSP/SWEAP/SPC with a cadence of ~28 s (the highest time resolution available during this time interval) and magnetic field magnitude B and magnetic field components in

(a) 15 Mar 2019/12:14 UT   (b) 13 Mar 2019/04:54 UT
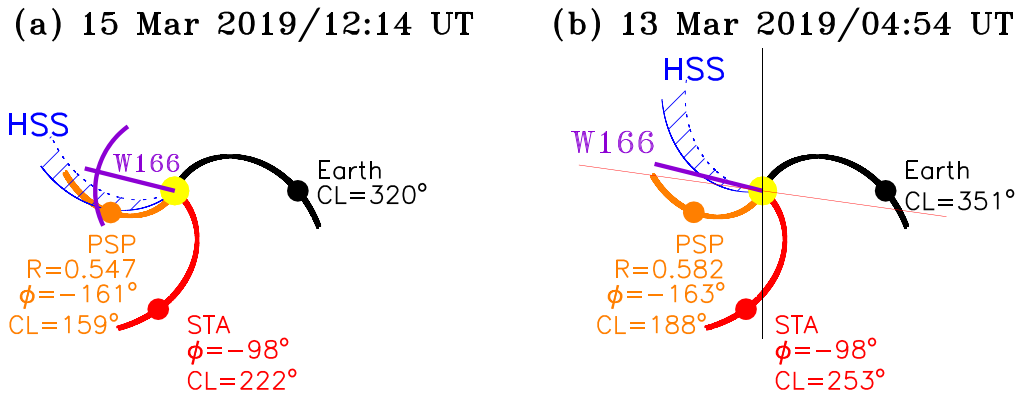

Figure 5. View from the north ecliptic pole showing the location of STEREO-A (STA; red symbol), Earth (black symbol), and PSP (orange symbol), (a) at 12:14 UT on 2019 March 15 when the leading edge of the MC reached PSP and (b) at 04:54 UT on 2019 March 13 when the parent SBO accelerated. CL and ϕ near each symbol indicate the CL and the HEEQ longitude of each observer. Also shown are nominal IMF lines connecting each spacecraft with the Sun (yellow circle at the center, not to scale) considering the solar wind measured at the time of the SBO-CME. The purple line indicates the longitude of the nose of the flux rope representing the SBO-CME (W166 as seen from Earth). The blue hatched region represents the corotating HSS observed in situ by PSP after the passage of the MC, and the purple arc in panel (a) represents the shocks observed in front of the ICME.

the RTN spacecraft coordinate system as collected by PSP/ FIELDS with a time cadence of 0.1 s. Figure 4 covers a period of ~11 minutes about ~3.25 hr before the arrival of the ICME leading edge. The two shocks, indicated by the two solid vertical lines, can be clearly identified by the abrupt jumps in B at 08:56:01 UT and 09:00:07 UT. There are enhanced magnetic field fluctuations for ~20 s upstream of both shocks. The plasma data do not show clear discontinuities at the shocks in all parameters, but the errors are also relatively large in N_p and T_p. Nevertheless, to obtain the "best-fit" shock parameters, we have applied a least-squares method to fit the full set of Rankine–Hugoniot conservation equations to the magnetic field and plasma measurements (Koval & Szabo 2008, 2010) using as upstream and downstream regions the time intervals 08:52:17–08:55:05 UT and 08:56:57–08:58:48 UT for the first shock, and 08:56:57–08:58:48 UT and 09:00:12–09:02:04 UT for the second shock, respectively. The solutions for the first shock are: normal vector direction $\boldsymbol{n} = (0.83 \pm 0.03, -0.12 \pm 0.04, 0.55 \pm 0.04)$ in RTN coordinates, angle between $\boldsymbol{n}$ and the upstream magnetic field $\theta_{Bn} = 46 \pm 2°$, shock speed $V_{\rm sh} = 370 \pm 135$ km s^{-1}, and fast magnetosonic Mach number $M_f = 2.0 \pm 2.4$. For the second shock, the solutions are: $\boldsymbol{n} = (0.72 \pm 0.06, \quad 0.01 \pm 0.02, \quad 0.70 \pm 0.06), \quad \theta_{Bn} = 60 \pm 2°$, $V_{\rm sh} = 376 \pm 34$ km s^{-1}, and $M_f = 2.1 \pm 0.3$. An estimation of the density r_n and magnetic field r_b compression ratios gives $r_n = 1.10 \pm 0.20$ and $r_b = 1.25 \pm 0.02$ for the first shock, and $r_n = 1.27 \pm 0.17$ and $r_b = 1.40 \pm 0.02$ for the second shock. These shock parameters would lie at the weaker ends of the distributions of shock parameters found by Lario et al. (2005) at 1 au and by Volkmer & Neubauer (1985) close to 0.5 au using Helios observations. These results suggest that the two shocks had similar properties, with the second shock being slightly stronger, although the parameters of the first shock have significantly larger uncertainties than those of the second shock. The normal directions of the two shocks point mostly southward from the radial anti-sunward direction (the latitude and longitude directions of the shock normals in the RTN coordinate system are $\Theta_n \sim -34°$ and $\Phi_n \sim 172°$ for the first shock and $\Theta_n \sim -44°$ and $\Phi_n \sim 179°$ for the second shock). The close proximity of the two shocks and their similar properties suggest a similar origin for the two shocks. The transition from the upstream to the downstream regime might have occurred in two steps rather than one, with the possibility

that at some other point in space and time, the shocks would have merged into just one.

3. Solar Origin of the ICME

In order to identify a possible candidate for the solar origin of the ICME observed in situ by PSP, we make use of concomitant remote-sensing observations of the solar corona by the Solar and Heliospheric Observatory (SOHO) and by the Ahead spacecraft of the Solar TErrestrial RElations Observatory (i.e., STEREO-A, henceforth STA). Figure 5(a) shows the distribution of these spacecraft and PSP, as seen from the north ecliptic pole, at the time when the PSP intercepted the MC leading edge. The black, red, and orange dots indicate the locations of Earth, STA, and PSP, respectively. The Carrington longitude (CL) and the longitude in the Heliocentric Earth EQuatorial (HEEQ) coordinate system (ϕ) of each spacecraft are indicated in Figure 5(a) next to each dot (following the same color scheme). A solar wind transient structure traveling at ~400 km s^{-1} takes about ~57 hr to travel from the Sun to 0.547 au assuming constant speed. Therefore, a candidate source for the MC at PSP would have erupted on the Sun early on 2019 March 13. Following the same scheme as Figure 5(a), Figure 5(b) shows the distribution of spacecraft at 04:54 UT on 2019 March 13 (the reason for this time will be discussed below). The thin straight red and black lines represent the plane of the sky for the coronagraphs on board STA and on board SOHO, respectively. A transient structure of solar origin observed later in situ by PSP should have been observed by STA above the east limb and would have been a farside event from the location of SOHO.

The Large Angle and Spectrometric Coronagraph Experiment (LASCO) on board SOHO (Brueckner et al. 1995) contains two white-light coronagraphs, C2 and C3, that cover the plane-of-sky distances 2–7 $R_\odot$ for C2 and 3.7–30 $R_\odot$ for C3 (e.g., St. Cyr et al. 2000). In this paper, data from LASCO C2 were processed with the dynamic separation technique (Morgan et al. 2012; Morgan 2015). This technique enables the separation of the dynamic and quiescent components in coronagraph images through a spatial-temporal deconvolution method. The method is based on the assumption that the quiescent corona is always radially smoother than the dynamic component, and so the structure of CMEs and
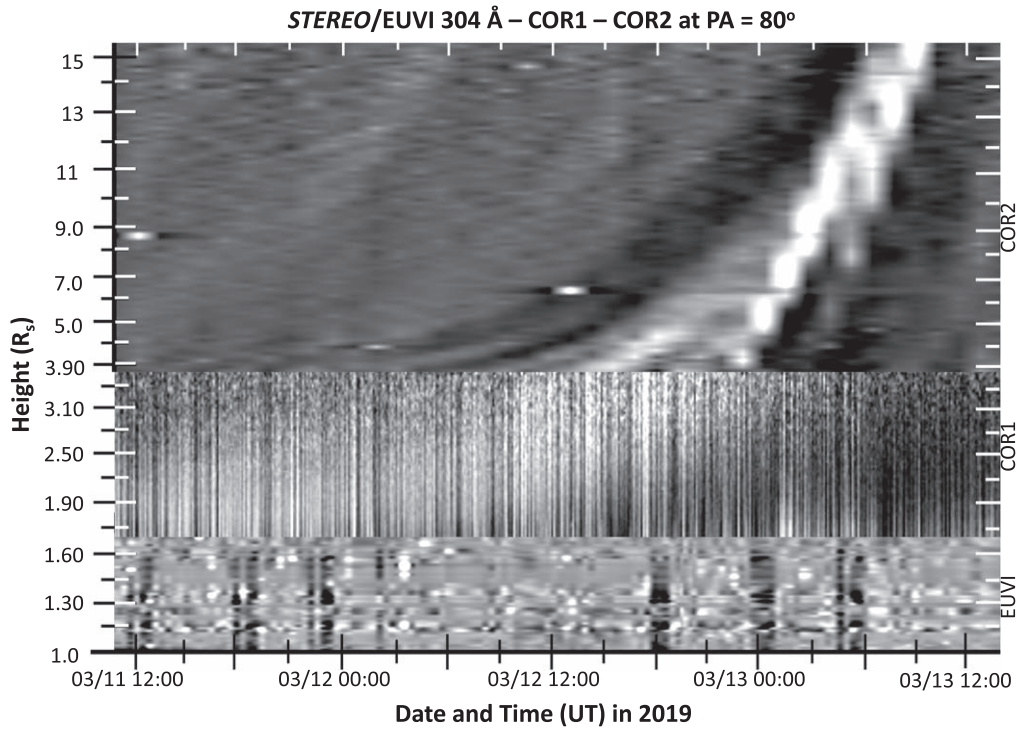
Figure 6. Height–time map showing structures in the corona from 1 to 15 $R_\odot$ generated from STA/SECCHI observations at PA = 80°, with EUVI data at the bottom of the plot, COR1 in the middle, and COR2 in the top half of the plot. The FOVs shown extend out to 1.7 $R_\odot$ for EUVI, from 1.7 to 3.9 $R_\odot$ for COR1, and from 3.9 to 15.5 $R_\odot$ for COR2. A structure in COR1 that crosses into the COR2 FOV is clearly seen.

other transients is revealed despite the presence of bright background streamers.

The Sun Earth Connection Coronal and Heliospheric Investigation (SECCHI; Howard et al. 2008) on board STA contains two white-light coronagraphs, COR1 and COR2, covering the heliocentric distances in the plane of the sky from 1.4 to 4.0 $R_\odot$ for COR1 and from 2.5 to 15.6 $R_\odot$ for COR2. SECCHI also contains an Extreme Ultraviolet Imager (EUVI; Wuelser et al. 2004) with a field of view (FOV) that extends from 1.0 to ~1.6 $R_\odot$ (depending on the wavelength). Unfortunately, for this event, STA was not well oriented to track structures propagating all the way to PSP with the two heliospheric imagers HI1 and HI2 of the SECCHI instrument, and data from these instruments have not been used here. In this paper, we use STA time-series observations from EUVI, COR1, and COR2. Using the standard calibration *SolarSoft* routine, we combine polarization sequence images into an estimate of polarized brightness and transform them into heliocentric polar coordinates. We smooth each time series using two normalized Gaussian kernels (a wide, then a narrow kernel) to suppress high-frequency noise, which is ever-present in COR1, and low-frequency variations, which are typically opaque dynamic structures in the images. To generate height–time profiles of the data, we re-bin the total brightness images into 100 regular height bins (spanning the FOV of the instrument for each time series of observations) and 72 angle positions. We then apply the Gaussian kernels at each binned polar-coordinate in each time series, thus resulting in a data cube of filtered time series with dimensions of PA× height× time, where PA is the position angle (measured counter-clockwise from solar north in the coronagraph and EUVI images). Radial slices of the filtered data are then extracted at selected PA bins to generate height–time plots. A normalization of the brightness amplitude with time is then applied for display

purposes, thus revealing the continuation of moving structures along the FOVs. For a detailed description of this methodology, see Alzate et al. (2020). Figures 6 and 7, as well as Figures A1 and A2 in the Appendix, were created following this methodology.

Figure 6 shows a height–time map combining observations collected by EUVI, COR1, and COR2 on board STA from 12:00 UT on 2019 March 11 to 12:00 UT on 2019 March 13. The map was generated using 304 Å images from EUVI and white-light COR1 and COR2 images for a radial slice at PA = 80°. In the EUVI portion (from 1 to 1.7 $R_\odot$), no apparent structure can be distinguished. The COR1 portion shows first a streamer brightening starting early on 2019 March 12 followed by an outward motion with an estimated plane-of-sky average speed of ~34 km s^{-1}. COR2 shows first an outward moving streamer brightening starting on midday of 2019 March 12 with an average plane-of-sky speed of ~97 km s^{-1}. The subsequent brighter and faster COR2 signature starting early on 2019 March 13 was moving outward with an estimated plane-of-sky speed measured between ~10 $R_\odot$ and 15 $R_\odot$ of ~276 km s^{-1}. The top row of Figure 7 shows coronagraph images from, left to right, SOHO/LASCO/C2, SOHO/LASCO/C3, and STA/SECCHI/COR2 at 05:00 UT on 2019 March 13 for C2, at 05:06 UT for C3, and at 05:08 UT for COR2. We have indicated with a white arrow the structure that most likely was the source of the ICME at PSP. Figures A1 and A2 and the online supporting animations visualize the evolution of the structures highlighted in Figures 6 and 7 as seen from COR1 and COR2.

The first Appendix movie built from COR1 images shows a brightening of the streamer belt over the east limb of the Sun in the COR1 FOV at position angles between ~75° and ~90° that commenced early on 2019 March 12. An outward expansion of material at the same range of position angles slowly moved
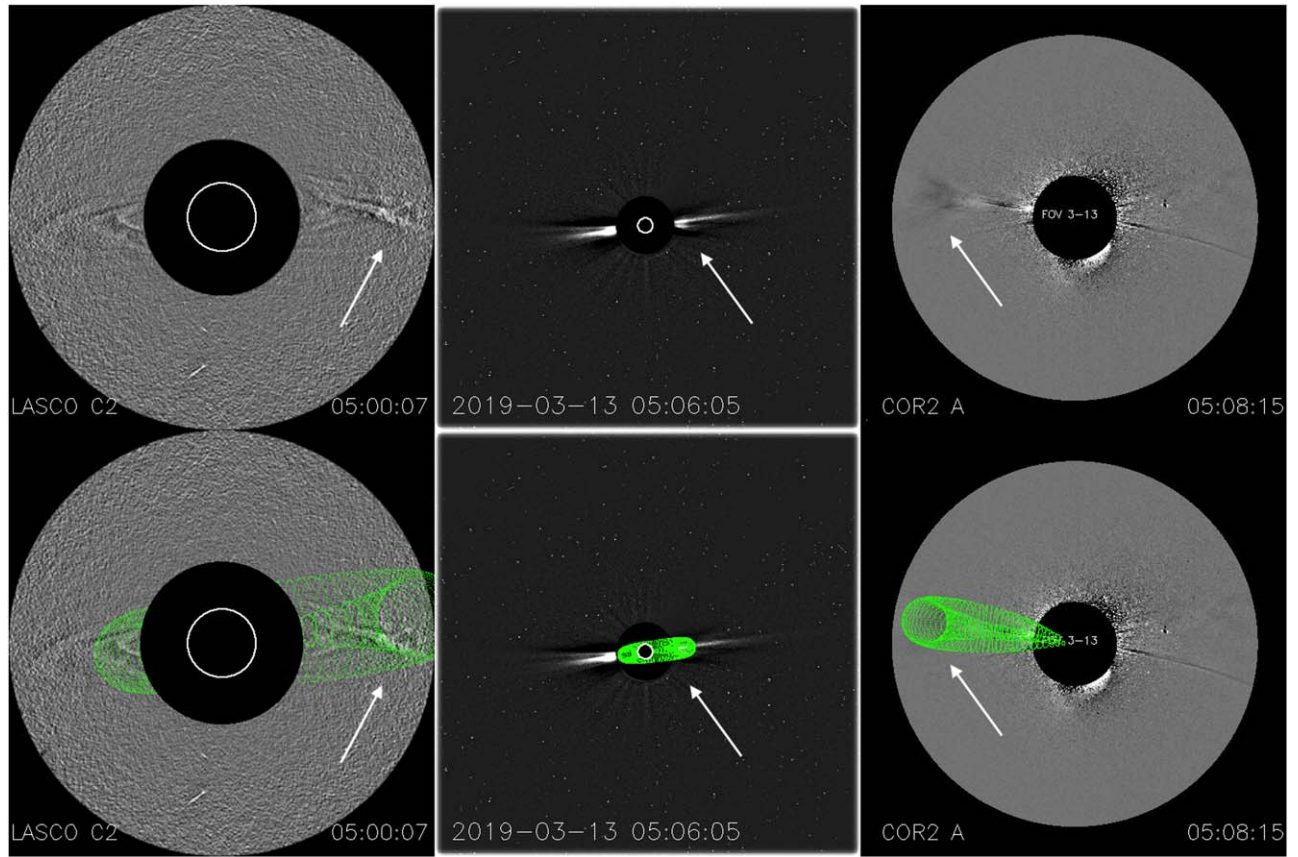
Figure 7. Coronagraph images and corresponding GCS modeling results (green grids) from left to right LASCO/C2, LASCO/C3, and STEREO-A/COR2. The time of the images is 05:00 UT for C2, 05:06 UT for C3, and 05:08 UT for COR2 on 2019 March 13. The black circle in the center is the occulting disk of the coronagraphs, and the white circle represents the solar disk. The white arrows indicate the main body of the SBO-CME flux rope in the COR2 and C3 images and the trailing part of the SBO-CME main body in the C2 image.

through the COR1 FOV starting on 2019 March 12 at ∼14:30 UT. The overlap between the COR1 and COR2 FOVs allows us to track the outward motion of this structure, which entered the COR2 FOV at ∼15:00 UT on 2019 March 12 as a slow streamer brightening. The second Appendix movie built from COR2 images allows us to follow these structures in the COR2 FOV. In COR1, after the brightening of the streamer, a transient structure crossed the FOV (best seen across the full length of the FOV at 20:00 UT on 2019 March 12) in the same radial direction as the structure that appeared in the COR2 FOV at ∼15:00 UT on the same day. This structure quickly accelerated as a new faster structure with typical signatures of an SBO that appeared in the COR2 FOV on 2019 March 13 at ∼00:54 UT. When the leading edge of the structure was already at a distance $\gtrsim 10\,R_\odot$, it accelerated again at ∼04:54 UT when new outflowing material (possibly caused by post-eruption reconnection, e.g., Webb & Vourlidas 2016, or by a new eruption) appeared in the COR2 FOV.

In the same range of PAs over which STA coronagraph images displayed the SBO, no clear signatures of structures lifting off from the Sun surface were seen in the EUVI images. This indicates that the main eruption that triggered the brightening of the streamer and the subsequent outward moving structure occurred most likely behind the solar limb as seen from STA and that it was seen to acquire larger speeds only when it was at high ($\gtrsim 10\,R_\odot$) altitudes over the east limb of the Sun. Considering the possibility that the subsequent outflowing material was associated with a second eruption or post-eruption reconnection,

the well-formed MC structure observed in situ by PSP (Figure 1) argues for a single structure directed toward this spacecraft rather than a compound structure formed by the coalescence of multiple structures, although the details of its solar origin in the lower corona cannot be completely determined.

The main body of the SBO-CME structure, indicated by a white arrow in the right panels of Figure 7, was easily seen moving eastward in the STA/SECCHI/COR2 FOV (see the second Appendix movie). In the C2 and C3 coronagraph images, a faint structure moving outward mostly over the west limb (indicated by the white arrow in the left and middle panels of Figure 7) was clearly seen. In fact, the LASCO/CME catalog of the Coordinated Data Analysis Workshop at cdaw.gsfc.nasa.gov/CME_list/ identified this CME first seen in the C2 FOV at 01:48 UT on 2019 March 13 as a narrow CME (plane-of-sky width = 18°) moving over the west limb of the Sun (at PA = 275°) with a plane-of-sky speed of 153 km s^{-1}. Actually, signatures of this structure over the east limb of the Sun (as seen from Earth) were also observed in LASCO C2 and C3 images. Therefore, the combined observations from SOHO and STA show that this was a farside event as seen from SOHO but an eastern event as seen from STA. This structure is an excellent candidate for the origin of the MC seen at PSP, not only because of the time when it was launched from the Sun but also because its general propagation direction is consistent with that required to encounter PSP (Figure 5).

We have used the graduated cylindrical shell (GCS) model (Thernisien et al. 2006, 2009) to reproduce the 3D geometry of

the structure using simultaneous coronagraph observations from SOHO and STA. The GCS model represents the idealized flux-rope structure of a CME and is composed of two cones describing the legs of a CME and a torus-like structure connecting these cones (see details in Thernisien 2011). The bottom row of Figure 7 shows the fits of the GCS model (green grid of points) to the CME observations from the two vantage points. The assumption is that a single structure formed the flux rope consistent with the simple well-formed ICME structure observed in situ by PSP. By using a sequence of images as co-temporal as possible from C2, C3, and COR2, the GCS model allows us to determine the direction of propagation, orientation, and height of the flux rope, and hence estimate its speed. We conclude that the CME evolved close to self-similarity, at least during the sequences of images from 02:54 UT on 2019 March 13 (when the leading edge of the structure was already above $\sim 10\,R_\odot$) to 06:43 UT (when the leading edge of the structure moved outside of the COR2 FOV). The propagation direction of the CME obtained from the GCS model did not change during this time interval, with the nose of the structure moving at $\sim 311\,\mathrm{km\,s^{-1}}$ and directed 166° west of the Sun–Earth line (CL = 156°) and 9° north of the ecliptic plane. The tilt angle of the CME flux rope was small ($\sim-6°$). Other parameters used in the GCS model are $\alpha = 50°$ and $\kappa = 0.148$ (see Figure 1 and Equations (1) and (2) in Thernisien et al. 2009, for the meaning of these parameters).

3.1. Comparison between the GCS Structure Close to the Sun and the In Situ MC 3D Reconstruction

In Figure 5, we have indicated with a purple line (at W166 with respect to Earth) the direction of the nose of the SBO-CME structure as inferred from the GCS fitting. This was directed 33° east of the longitude of PSP on 2019 March 15 at 12:14 UT when the leading edge of the ICME reached PSP. By assuming a self-similar expansion of the GCS flux rope to the PSP heliocentric distance, we can assess whether PSP could have intercepted this structure. Figure 8 shows the GCS flux rope expanded so that it encounters PSP. The long black arrow indicates the direction of the nose of the GCS structure in the HEEQ coordinate system (the green and red straight lines indicate the radial direction toward Earth and STA, respectively). The figure has been generated following the method described by Gonzàlez-Àlvarez (2019). It shows that, under the assumption of a self-similar expansion of the GCS structure, PSP would have intercepted the western leg of the flux rope. This configuration is consistent with the imbalance in the BDE flows observed within the ICME with a stronger outward electron flux (see Figure 2(m) and Section 2).

We have overplotted in Figure 8 the purple cylinder that represents the structure of the MC measured in situ and inferred by the EC model described in Section 2.1. The dashed black line in Figure 8 indicates the axis of the cylinder, and the orange line indicates the radial direction from the Sun to PSP (located within the cylinder). The orientation of the axis of the EC model flux rope is consistent with PSP intercepting the leg of the GCS flux rope, though the cross section of the EC flux rope (with a radius of only 0.0129 au) is much smaller than the cross section of the expanded GCS structure. In fact, the radius of the self-similarly expanded GCS structure, when its nose reached 0.547 au, was about 0.070 au along its axis of symmetry and 0.068 au at the portion intercepted by PSP
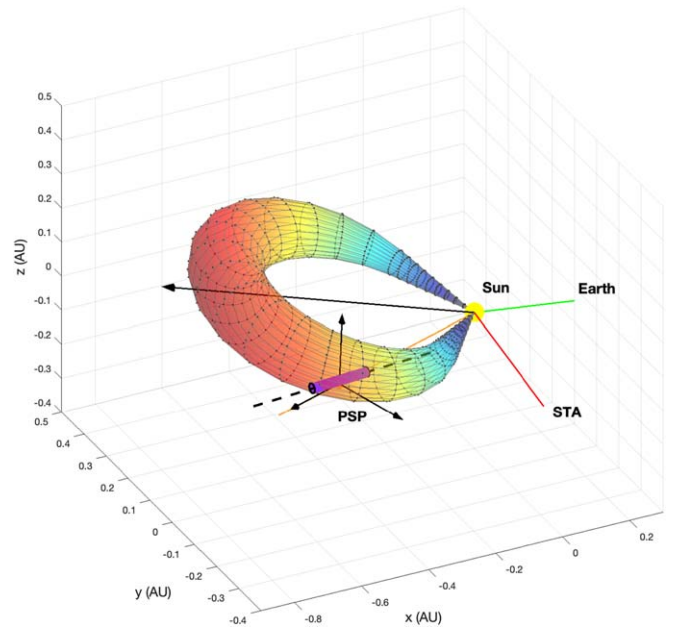

Figure 8. GCS fit to the initial CME (colored hollow croissant structure) self-similarly expanded to the distance where it intercepted PSP compared with the EC reconstruction of the MC (purple cylinder) in the HEEQ coordinate system. The orange, green, and red straight lines indicate the radial direction toward PSP, Earth, and STA, respectively. The position of PSP is within the cylinder structure. The long black arrow indicates the direction of propagation of the nose of the GCS structure, and the dashed straight black line indicates the axis of the MC according to the EC model.

(separated 33° with respect to the GCS nose direction). The size of the flux rope inferred from in situ observations is a factor of $\sim$5 smaller than the expanded GCS structure. Possible reasons for such a discrepancy include the fact that in situ observations are only made along a 1D cut through the structure. For this specific case, PSP moved just along one leg of the flux rope, making it difficult to infer the radial width of the flux rope. Additionally, the self-similar expansion of the GCS structure assumed in Figure 8 neglects the effects that the solar wind background medium might have had on both the ICME trajectory and shape, including processes of distortion, expansion, compression and even rotation that complicate the comparison between remote sensing and 3D MC morphology reconstruction from in situ measurements (e.g., Nieves-Chinchilla et al. 2012). In particular, the HSS observed after the MC passage (Figure 1) might have interacted with the MC and hence compressed and changed its shape. In order to investigate the possible interaction between the ICME and the HSS, it is essential to determine the origin of the HSS with respect to the trajectory of the ICME (see Section 4).

4. ICME Evolution in Interplanetary Space

In the absence of remote-sensing observations to track the ICME all the way from the corona to PSP, we have to hypothesize how interaction with the background medium, in particular with the following HSS, might have influenced the propagation of the ICME. To do so, we need to determine first the origin of the HSS with respect to the site where the SBO-CME was launched and then use MHD simulations of the ICME propagation through the solar wind.
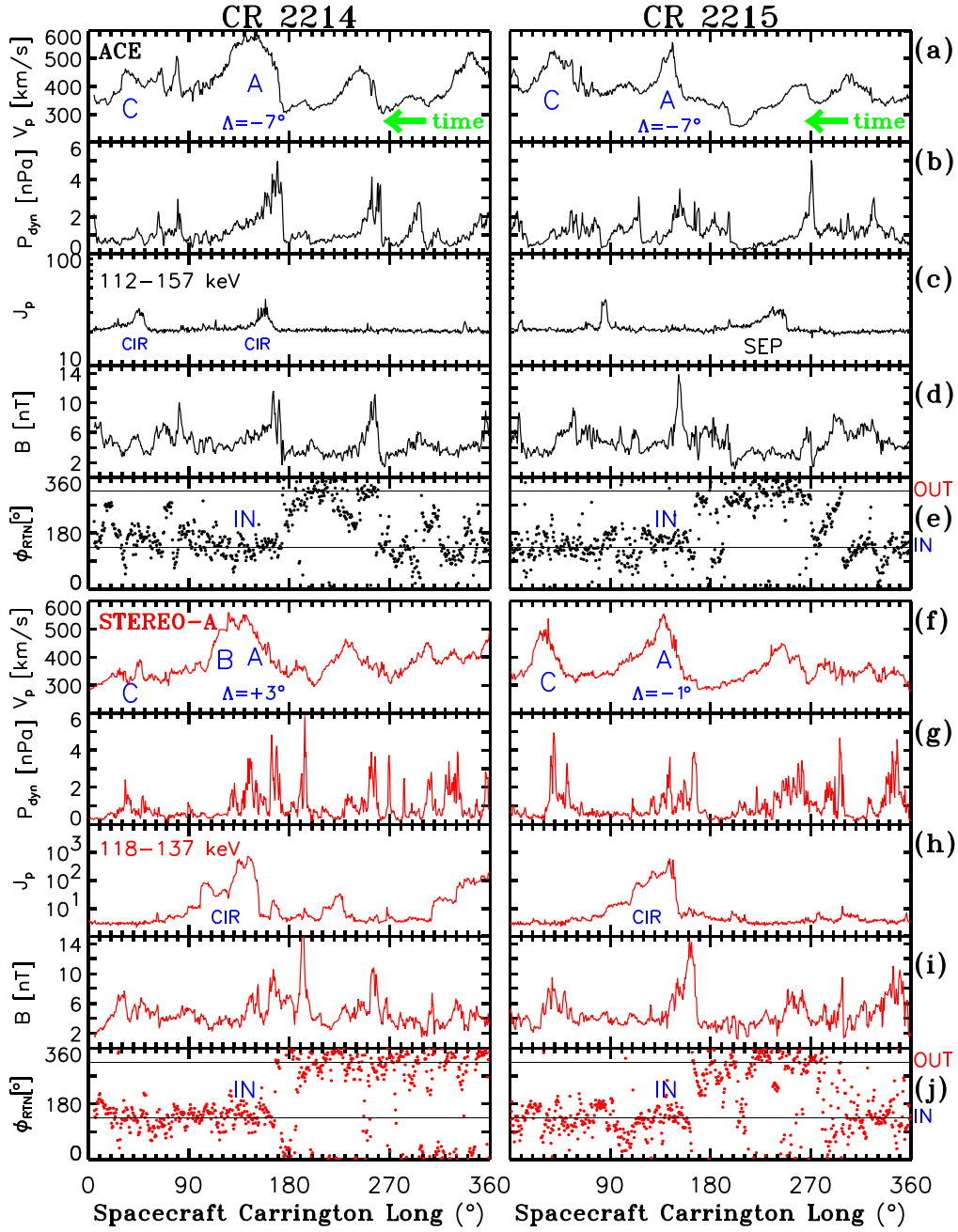
Figure 9. From top to bottom, (a) solar wind proton velocity V_p, (b) solar wind dynamic pressure P_{dyn}, (c) ∼120 keV ion intensities J_p, (d) magnetic field magnitude, and (e) magnetic field azimuth angle in the spacecraft-centered RTN coordinate system as measured by SWEPAM, EPAM, and the Magnetic Field Experiment on board ACE at 0.99 au; (f) solar wind proton velocity V_p, (g) dynamic pressure P_{dyn}, (h) ∼120 keV ion intensities J_p, (i) magnetic field magnitude, and (j) magnetic field azimuth angle in the spacecraft-centered RTN coordinate system as measured by PLASTIC, SEPT, and the Magnetic Field Experiment on board STA at 0.96 au as a function of the spacecraft CL during CRs 2214 (left) and 2215 (right). Time runs from right to left. Times considered for STA data are from 2019 February 5 at 15:51 UT to 2019 March 5 at 01:00 UT in the left panels and from 2019 March 5 at 01:00 UT to 2019 April 1 at 09:45 UT in the right panels. Energetic particle intensities J_p are given in units of particles $(cm^2 \, s \, sr \, MeV)^{-1}$. The letter A identifies an inward polarity high-speed stream sequentially observed at L1 and STA, and B and C indicate additional HSSs. Λ is the heliolatitude of each spacecraft during the passage of this high-speed stream. The CIR and SEP labels in panels (c) and (h) identify the energetic particle enhancements associated with the passage of the high-speed streams and an SEP event observed by ACE on 2019 March 20.

4.1. The Origin of the Post-MC High-speed Stream

We first consider whether the HSS was corotating with the Sun, in particular whether it was observed at similar CLs at PSP, STA, and near-Earth spacecraft on adjacent solar rotations. Figure 9 shows the solar wind proton speed (V_p), the dynamic pressure (P_{dyn}), the intensity (J_p) of ∼120 keV ions, the magnetic field magnitude, and the magnetic field azimuthal angle in the RTN coordinate system as measured by

the Advanced Composition Explorer (ACE) located near the Earth–Sun Lagrangian L1 point (black plots in panels (a) to (e)) and by STA (red plots in panels (f) to (j)) as a function of the spacecraft CL for Carrington rotations (CRs) 2214 (left panels) and 2215 (right panels). At that time ACE was located at 0.99 au from the Sun and STA at 0.96 au. Magnetic field data shown in Figure 9 were collected by the magnetometers on board ACE (Smith et al. 1998) and STA (Acuña et al. 2008). Energetic particle data were collected by the Electron, Proton,

and Alpha Monitor (EPAM) on ACE (Gold et al. 1998) and the Solar Electron and Proton Telescope (SEPT) on STA (Müller-Mellin et al. 2008), whereas the solar wind parameters used in Figure 9 were measured by the Solar Wind Electron, Proton, and Alpha Monitor (SWEPAM) on ACE (McComas et al. 1998) and the Plasma and Suprathermal Ion Composition (PLASTIC) on STA (Galvin et al. 2008). CR 2214 spans from 2019 February 13 at 04:00 UT to 2019 March 12 at 11:57 UT, and CR 2215 from 2019 March 12 at 11:57 UT to 2019 April 08 at 19:06 UT. The ACE data correspond exactly to these time periods, whereas the STA periods include observations from adjacent rotations. The ICME event at PSP occurred early on CR 2215 but at a longitude almost diametrically opposed to Earth (see Figure 5). Therefore, both CR 2214 and CR 2215 time intervals are relevant to determine the origin of the HSS and hence the conditions under which the ICME propagated toward PSP.

Figure 9 displays a relatively fast ($\gtrsim 500\,\mathrm{km\,s^{-1}}$) recurrent solar wind stream (labeled A in Figures 9(a) and (f)) with inward field polarity (Figures 9(e) and (j)) and with solar wind speed maximizing around CL $\sim 140°$–$150°$. This fast stream was also clearly observed by ACE and STA during the two prior rotations (not shown here). The characteristics of this fast stream varied from CR 2214 to CR 2215 and also with the heliolatitude of the spacecraft that observed the stream (indicated by the Λ value in Figures 9(a) and (f)). Whereas at southern latitudes (i.e., $\Lambda = -7°$ for ACE in both CRs and $\Lambda = -1°$ for STA in CR 2215) the solar wind speed increased abruptly with the arrival of the stream A, at northern latitudes (i.e., $\Lambda = +3°$ for STA in CR 2214) V_p rose more gradually. In fact the fast stream at STA during CR 2214 showed an extended duration with a second solar wind speed peak at CL $\sim 125°$. We have indicated this fast solar wind stream extension by the letter B in the left panel of Figure 9(f). We attribute some of the differences between STA and ACE in CR 2214 to the different latitudes of the two spacecraft. The significant latitudinal structure of high-speed streams in the inner heliosphere was revealed by the Helios spacecraft, which showed differences in the HSS structure when separated in latitude by just a few degrees (e.g., Schwenn et al. 1978, 1981). At 1 au, the dual STEREO observations also showed this latitudinal effect (e.g., Jian et al. 2019). Variability from one rotation to the next or even during rotations can also arise from changes in the source CHs, which might account for stream A becoming narrower in CR 2215. Additionally, we also identify with the letter C in Figure 9 an inward polarity high-speed stream at CL $\sim 30°$–$40°$ observed mostly at southern latitudes by ACE in both CRs and by STA in CR 2215.

In Figures 9(c) and (h), we have identified with the label CIR the energetic particle increases observed in association with the passage of these high-speed streams. These particle increases were observed mostly after the passage of the compressed region formed in front of the fast solar wind streams as typically observed in CIR events at 1 au (e.g., Mason & Sanderson 1999). Note the different instrumental background for ACE/EPAM and STA/SEPT, and the fact that these two instruments are not necessarily inter-calibrated. An additional solar energetic particle (SEP) event was observed by ACE on 2019 March 20 (Figure 9(c)).

The two top panels of Figure 10 show synoptic maps of the EUV emission from the solar corona, for (a) CR 2214 and (b) CR 2215, created from 193 Å bandpass images from the Atmospheric Imaging Assembly on board the Solar Dynamics

Observatory (SDO/AIA; Lemen et al. 2012). We have indicated with the letters A, B, and C the CHs that were more likely the origin of the solar wind streams identified in Figure 9. The origin of the recurrent fast stream A was most likely a CH that crossed central meridian at Earth around 2019 February 25 and 2019 March 26. This CH was observed on several rotations prior to CR 2214, but it became much narrower in CR 2215 (Figure 10(b)). We have identified with the letter B an equatorial extension of the CH A in Figure 10(a), which became very small and most likely detached from A in CR 2215. At CL $\sim 90°$, we have also identified another CH with the letter C as shown in Figures 10(a) and (b).

Predictive Science, Inc. have constructed photospheric magnetic field synoptic maps for each CR (www.predsci.com/hmi/coronal_hole_map.php) using magnetogram observations centered at the Earth's central meridian collected by the Helioseismic and Magnetic Imager (HMI) on board SDO (Scherrer et al. 2012), over a ~ 27 day period. Figures 10(c) and (d) display CH maps for CR 2214 and CR 2215 based on regions of open field lines, which are color coded according to the observed underlying photospheric field (red for outward and blue for inward). The gray regions represent closed field regions. Note that in the construction of these maps, interpolation of the original magnetogram data and smoothing to a uniform grid have been performed (see Linker et al. 2017, for a description of the CH map construction process). The black, red, and orange vertical dashed lines in Figure 10 indicate the central meridian longitudes from the point of view of Earth, STA, and PSP, respectively, at 04:54 UT on 2019 March 13. These central meridian longitudes move to the left with time as indicated by the CL values of these locations in Figure 5(a). As expected, the CHs in the Predictive Science maps are generally consistent with those identified in the AIA observations. The equatorial extension of the southern CH with an inward magnetic field at CL $\sim 180°$ can be identified with the CH A in Figures 10(a) and (b) as the origin of the fast stream A ($\sim 500\,\mathrm{km\,s^{-1}}$) observed in situ by ACE at CL $\sim 150°$. The offset between the CL of the source of the fast streams and the CL of the spacecraft that observes the in situ passage of the fast stream is due to the finite transit time of the solar wind to travel from the Sun to the spacecraft as the Sun rotates. The extension of the CH origin of the fast stream A to lower CL values ($\sim 150°$) and equatorial latitudes (labeled B in Figures 10(c) and (d)) may be the origin of the fast-stream extension B observed in situ by STA in CR 2214 when the spacecraft was at northern latitudes ($\Lambda = +3°$). The effects of the stream B at southern latitudes ($\Lambda = -7°$) are diminished. Figures 10(a)–(b) and 10(c)–(d) show that the topology of this equatorial CH extension changed from CR 2214 to CR 2215, with the portion of B near CL $\sim 150°$ becoming smaller in CR 2215. Whether the CHs A and B were separate or part of the structure that evolved in latitude and longitude with time depends on the approximations made in the processing of the CH maps. We attribute the changes observed in the solar wind speed and magnetic field profiles in Figure 9 between CR 2214 and CR 2215 to both the temporal evolution of the CHs and to STA moving in latitude from $\Lambda \sim +3°$ in CR 2214 to $\Lambda \sim -1°$ in CR 2215.

PSP was located at CL $= 153°$ on 2019 March 16 at 00:00 UT when the maximum solar wind speed of $\sim 500\,\mathrm{km\,s^{-1}}$ was observed by PSP after the ICME passage (Figure 1(a)), and at CL $= 161°$ on 2019 March 15 at 09:00 UT when the two
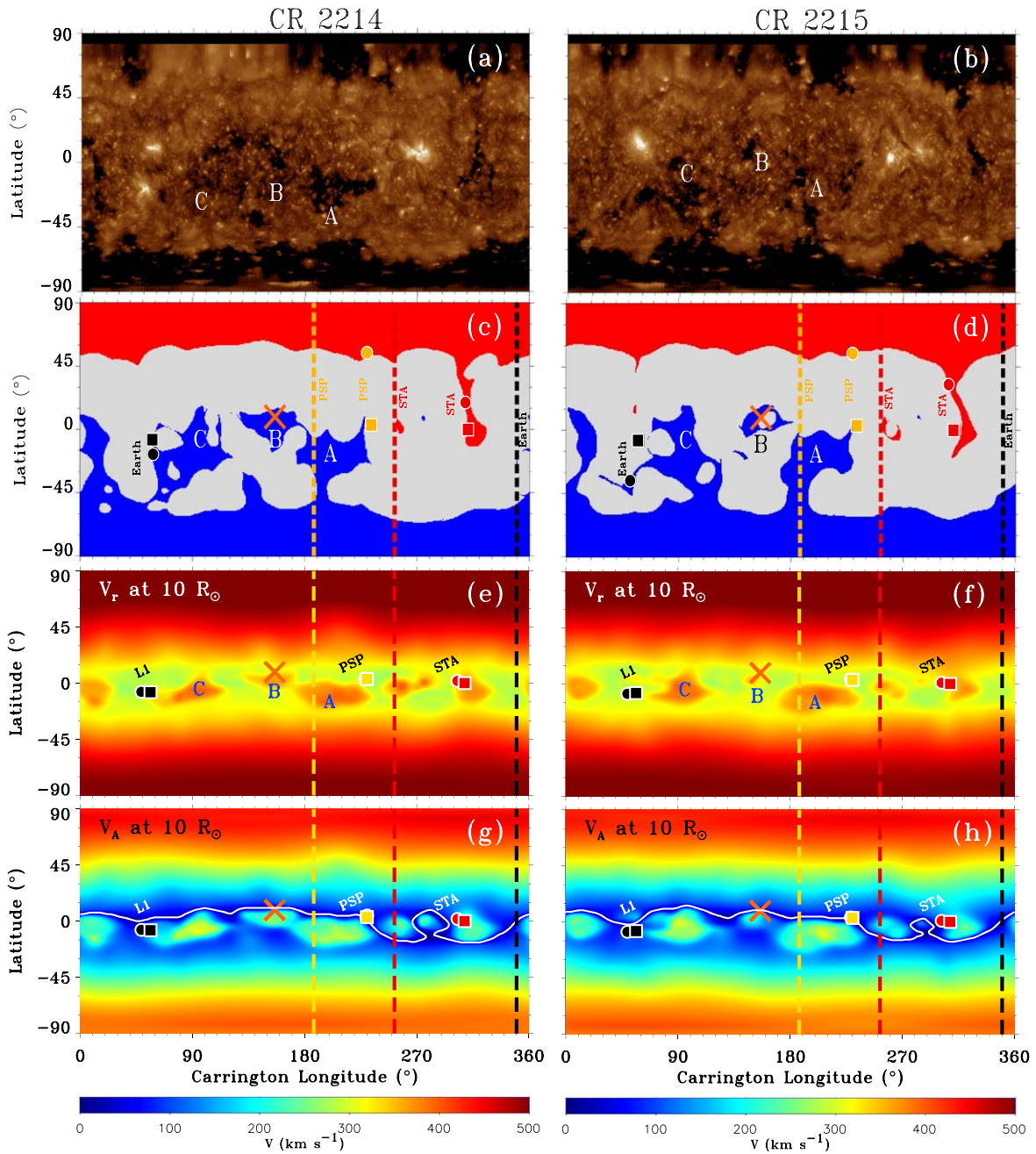
Figure 10. From top to bottom: synoptic maps built from SDO/AIA 193 Å observations for (a) CR 2214 and (b) CR 2215 as downloaded from sdo.gsfc.nasa.gov/assets/img/synoptic. CL-heliolatitude maps obtained from predsci.com/hmi displaying: (c–d) the CH structure at 1 $R_\odot$ used as a magnetic field input boundary condition in the "Magnetohydrodynamic Around a Sphere model in its Thermodynamic" (MAST) model (gray areas represent closed field regions, whereas blue and red areas represent inward and outward open field regions (i.e., CHs), respectively); (e–f) solar wind radial speed V_r at 10 $R_\odot$; and (g–h) Alfvén speed V_A at 10 $R_\odot$ as obtained by MAST in (left) CR 2214 and (right) CR 2215. In panels (c–h), the vertical dashed lines indicate the CLs of PSP (yellow), STA (red), and Earth (black) at 04:54 UT on 2019 March 13 when the SBO accelerated. The yellow, red, and black dots indicate the footpoints of the magnetic field lines connecting to PSP, STA, and Earth obtained from the MAST solutions on the photosphere (c–d) and at 10 $R_\odot$ (e–f and g–h). The yellow, red, and black squares indicate the footpoints of nominal Parker spiral magnetic field lines connecting to PSP, STA, and Earth all the way to the photosphere (c–d) and at 10 $R_\odot$ (e–f and g–h). The orange cross indicates the direction of the nose of the SBO as represented by GCS applied at helioradii above 10 $R_\odot$. Note that the coronal field configuration around the site of the SBO changed its configuration between CR 2214 and CR 2215. The white lines in panels (g) and (h) indicate the neutral line. Although strictly speaking the event occurred during CR 2215, the site of the SBO was located on the backside of the Sun as seen from Earth. Therefore, the MAST solution for CR 2215 did not implement the input photospheric magnetic field until late in the solar rotation.

shocks preceding the ICME arrived at PSP (Figure 4). The latitude of PSP ($\Lambda = +3°$) was similar to that of STA in CR 2214. It is therefore straightforward to associate the HSS observed by PSP with the combination of the fast streams A and B as observed by STA in CR 2214 (Figure 9(f)). The major difference is the MC at PSP embedded in the gradual solar wind speed increase. In addition, Figures 9(e) and (j) display a change of field polarity from outward to inward immediately preceding fast stream A at CL ~ 170° on both CRs well before the peak of the solar wind speed. The corresponding polarity change occurred at PSP on 2019 March 14 at ~21:00 UT (Figure 1(h)) when at a similar CL (167°).
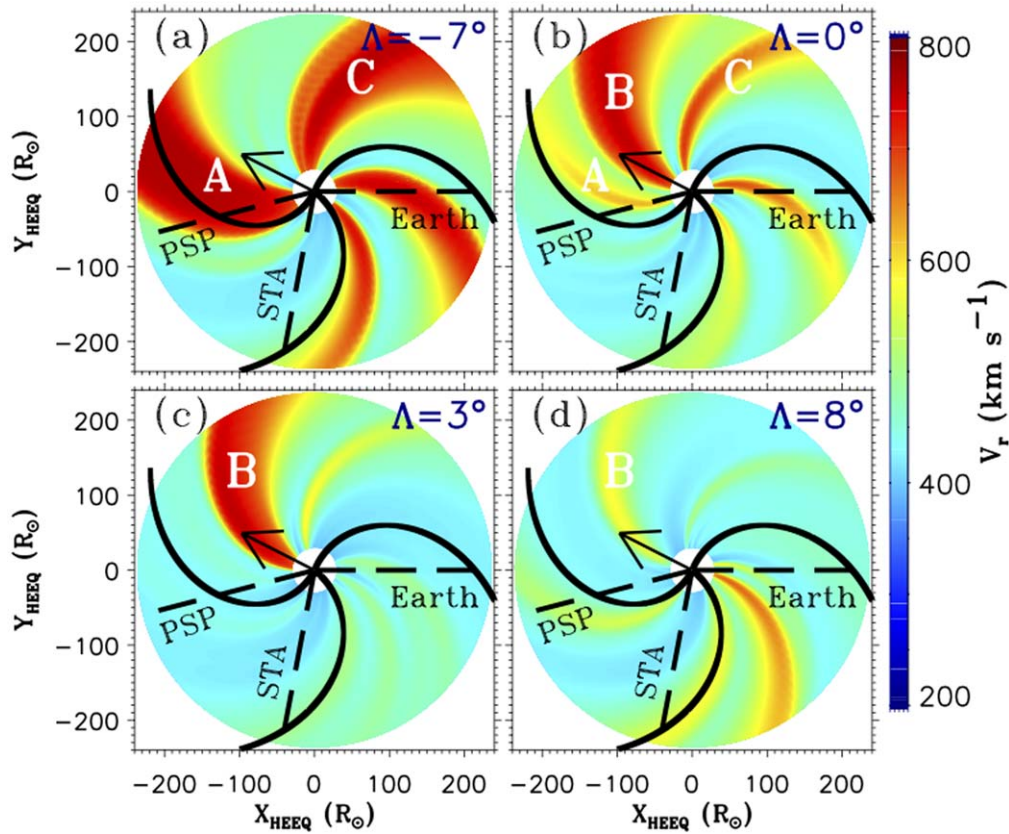
Figure 11. Solar wind velocity distribution at different heliolatitudes Λ in the HEEQ coordinate system as derived by the 3D PredSci MHD simulation for CR 2214. The dashed black straight lines indicate the direction toward PSP, STA, and Earth, and the black solid lines show the nominal Parker spiral IMF lines toward each spacecraft. Whereas at southern latitudes the high-speed solar wind streams A and C are clearly noticeable, moving northward in latitude, the high-speed stream B becomes more prominent close to the equator ($\Lambda \pm 3°$) and then fades above $\Lambda = +3°$.

MHD simulations of the corona can help characterize the coronal medium through which the SBO-CME initially propagated. We use the 3D MHD simulations developed by Predictive Science, Inc., in the context of the "Magnetohydro-dynamic Around a Sphere model in its Thermodynamic" version (MAST; Lionello et al. 2009) to analyze the global plasma configuration of the corona at the time of the SBO-CME. These simulations (available at predsci.com) are based on specific CRs and use as input photospheric magnetic field synoptic maps built up from the same HMI magnetograms used to create the open field plots in Figures 10(c) and (d). Figures 10(e) and (f) (10(g) and (h)) show the radial component of the solar wind speed V_r (the Alfvén speed V_A) as a function of CL and heliolatitude at a height of $10\,R_\odot$ as obtained from the MAST model applied to SDO/HMI observations for CR 2214 (left) and CR 2215 (right). The vertical dashed orange, red, and black lines indicate the central meridian longitude as seen from PSP, STA, and Earth on 2019 March 13 at 04:45 UT, respectively. The yellow, red, and black squares indicate the coordinates of the interception of the nominal Parker spiral IMF lines connecting with PSP, STA, and Earth with a sphere at $10\,R_\odot$. The yellow, red, and black dots indicate the coordinates of the intercept of a sphere at $10\,R_\odot$ with the field lines connecting with PSP, STA, and Earth as provided by the MAST model. To compute these field lines, we first use the spacecraft position and the solar wind speed measured by each spacecraft at 04:45 UT on 2019 March 13 to compute nominal Parker spiral IMF lines up to a distance of $30\,R_\odot$, and then use the coronal field configuration provided by MAST. The squares

and dots in Figures 10(c) and (d) have the same meaning but at a height of $1\,R_\odot$.

The orange cross in Figure 10 indicates the direction of the nose of the GCS flux rope obtained from fitting coronagraph images above $10\,R_\odot$ (Figure 7). Since this direction lies above the neutral line (indicted by the white line in Figures 10(g) and (h)), and streamers form above the neutral line, this supports an SBO origin for this event. Note that the event occurred during solar minimum conditions and the streamer belt was relatively flat, forming the base of the large-scale HCS. The direction of the leading edge of the GCS flux rope lies north of fast stream B in Figure 10(e) in which V_r reaches values $\gtrsim 400\,\mathrm{km\,s^{-1}}$, whereas the fast streams A and C lie southwest and southeast of the GCS nose direction, respectively. In CR 2215 (Figure 10(f)), stream B is weaker and narrower, introducing some uncertainty in the precise CH configuration at the time of the SBO-CME eruption.

Figure 11 shows the heliospheric extension of the MAST model for CR 2214 as obtained by the polytropic heliospheric model by Riley et al. (2011, 2012). In particular we show the solar wind $X–Y$ distribution in HEEQ coordinates at different latitudes Λ from (a) south ($\Lambda = −7°$) to (d) north ($\Lambda = +8°$). The dashed black lines indicate the radial directions toward PSP, STA, and Earth at 04:54 UT on 2019 March 13, and the solid lines are nominal Parker IMF field lines connecting to each spacecraft as indicated in Figure 11 (spacecraft would be located at the intersection between dashed and spiral lines). The black arrow identifies the longitude of the nose of the GCS flux rope. There is evidently a substantial change in the solar wind

structure over this latitude range. Whereas at southern latitudes the fast streams A and C are broad and conspicuous (Figure 11(a)), moving northward, these two streams become less visible while fast stream B becomes more evident up to a latitude $\Lambda = +3°$ (where PSP was located). Above this latitude (Figure 11(d)), the fast stream B weakens again. Thus, we would expect that, at the latitude of the GCS flux-rope nose (9°), the effects of the fast stream B must be less important than at the latitude of PSP.

Unfortunately, the spacecraft configuration (Figure 5) did not allow for a clear identification of the eruption site of the CME on the solar photosphere, as no EUV signatures were observed in the low corona above the limb prior to the SBO-CME eruption (Section 3). If the CME originated at a low altitude close to the solar surface, the presence of CHs nearby (i.e., close to the orange cross in Figure 10) may have helped establish its final propagation direction at higher altitudes (e.g., Mäkelä et al. 2013). The influence of the background medium on the propagation of CMEs is usually observed in the form of deflections that usually happen close to the Sun (usually at distances $<2 R_\odot$ above the solar surface; e.g., Kay & Opher 2015) and are attributed to magnetic field gradients in the low corona (e.g., Liewer et al. 2015). Thus, the presence of the CHs south of the direction of the nose of the flux rope derived from the GCS model and the high magnetic field (as shown by the high V_A values south of the orange cross in Figure 10(g)) may have contributed to the northern direction of propagation of the CME. If the SBO-CME originated at higher altitudes, its nose direction was already determined by the position of the neutral line. As the ICME expanded in IP space, the northern portions of the ICME might have freely propagated in a relatively undisturbed medium (Figure 11(d)), whereas the southern portions might have interacted with the combination of the fast streams A and B (Figure 11(b)). Note in Figure 10 that the PSP central meridian at 04:54 UT on 2019 March 13 (i.e., at the time when the original SBO-CME accelerated), indicated by the orange dashed vertical line in Figure 10, crosses CH A, suggesting that the portion of the ICME originally directed toward PSP interacted with fast stream A.

4.2. ADAPT-WSA-ENLIL-cone Simulation

In order to determine whether the initial SBO-CME, with the properties inferred from the coronagraph observations (Section 3), was able to reach PSP under a structured solar wind, we proceeded to perform ADAPT-WSA-ENLIL-Cone MHD simulations readily available to the heliophysics community in the NASA Community Coordinated Modeling Center at ccmc.gsfc.nasa.gov. The numerical 3D MHD code ENLIL (Odstrcil et al. 2004) uses the output from the Wang–Sheeley–Arge (WSA) model (Arge et al. 2004) to generate the structured background solar wind above a heliocentric distance of 21.5 $R_\odot$. The WSA model uses synoptic solar magnetic field maps derived from magnetogram observations. WSA is based on (1) the coupling between the potential field source surface and the Schatten current sheet models of the solar corona (Schatten et al. 1969; Schatten 1971), and (2) the use of an empirical relationship between the solar wind radial velocity and magnetic field expansion factor that depends on the distance of a solar wind source region from the nearest CH boundary (Arge et al. 2004). In principle, the WSA model can use as input synoptic magnetograms from any observatory. For this study, we use an intermediate step based on applying first the Air Force Data Assimilative Photospheric Flux Transport

(ADAPT) to an ensemble of SDO/HMI magnetograms (Arge et al. 2010; Henney et al. 2012; Hickmann et al. 2015). ADAPT produces an ensemble of 12 model realizations that are based on varying the model parameters used in the photospheric magnetic flux transport within a range of uncertainties that accounts for photospheric flows. These provide 12 synchronic maps of the Sun's surface magnetic field that are used by WSA as boundary conditions to derive the coronal field out to 21.5 $R_\odot$. Field line tracing from 21.5 $R_\odot$ down to the photosphere is used to determine open and closed field regions at 1 $R_\odot$ and thus generate CH maps (Wallace et al. 2019).

We have applied ADAPT-WSA to a number of synoptic magnetogram maps built from SDO/HMI magnetograms during CR 2214. Realization #8 applied to a synoptic map where the last SDO/HMI magnetogram used was that from 2019 March 11 at 20:00 UT, best reproduced the CH structure shown in Figure 10(a) and the high-speed streams configuration described in Section 4.1. Figure 12(a) shows the CH map inferred from the ADAPT-WSA model with a 2° resolution in both latitude and longitude. In comparison with Figures 10(c) and (d), ADAPT-WSA provides fragmented CHs. In the generation of the CH maps shown in Figures 10(c)–(d) and 12(a), different smoothing, re-gridding, and interpolation techniques are used, which may lead to these different configurations (Linker et al. 2017). Figure 12(b) shows the solar wind speed map generated by the WSA model that is used as input to the ENLIL code at its inner boundary (i.e., at 21.5 $R_\odot$). The fragmented structure of the CHs translates into patchy islands of fast solar wind that contrast with the large-scale areas of high-speed flows shown in Figures 10(e) and (f) owing to the less smoothing involved in building the CH map shown in Figure 12(a). We have identified with letters A, B, and C the patches of higher solar wind speed in Figure 12(b) arising from inward polarity CHs in Figure 12(a) that are associated with the speed streams described in Section 4.1. At equatorial latitudes, the speed patch B seems to be separated from the fast solar wind originating from the southern polar CH, whereas the speed patch associated with the CH A in Figure 12(a) becomes a small entity that, in the ENLIL simulation, becomes merged with the southern polar CH solar wind at lower latitudes.

In order to incorporate the ICME into the background medium generated by the ADAPT-WSA-ENLIL model, we use the "cone" approach (e.g., Odstrcil et al. 2004, 2020; Mays et al. 2015, and references therein), which assumes that close to the Sun the ICME propagates with constant angular width. The kinematic properties of the CME inferred from coronagraph images are used to define the properties of a CME-like, spheriod hydromagnetic cloud structure (i.e., a pressure pulse) that is launched into the background solar wind and magnetic field. The input parameters that specify the CME cloud at the inner boundary of the ENLIL code are the time of its passage by 21.5 $R_\odot$, the longitude and latitude of the CME, the major and minor radii of the CME (i.e., r_{major} and r_{minor} related to the GCS parameters as specified in Equations (31) and (32) of Thernisien 2011), the tilt of the CME, and its radial speed. The GCS parameters described in Section 3 provide 9° and 166° for the latitude and longitude of the nose of the CME, $r_{major} = 42°$ and $r_{minor} = 14°$ for the dimension of the CME, a tilt of $-6°$, and a radial speed of 311 km s^{-1}.
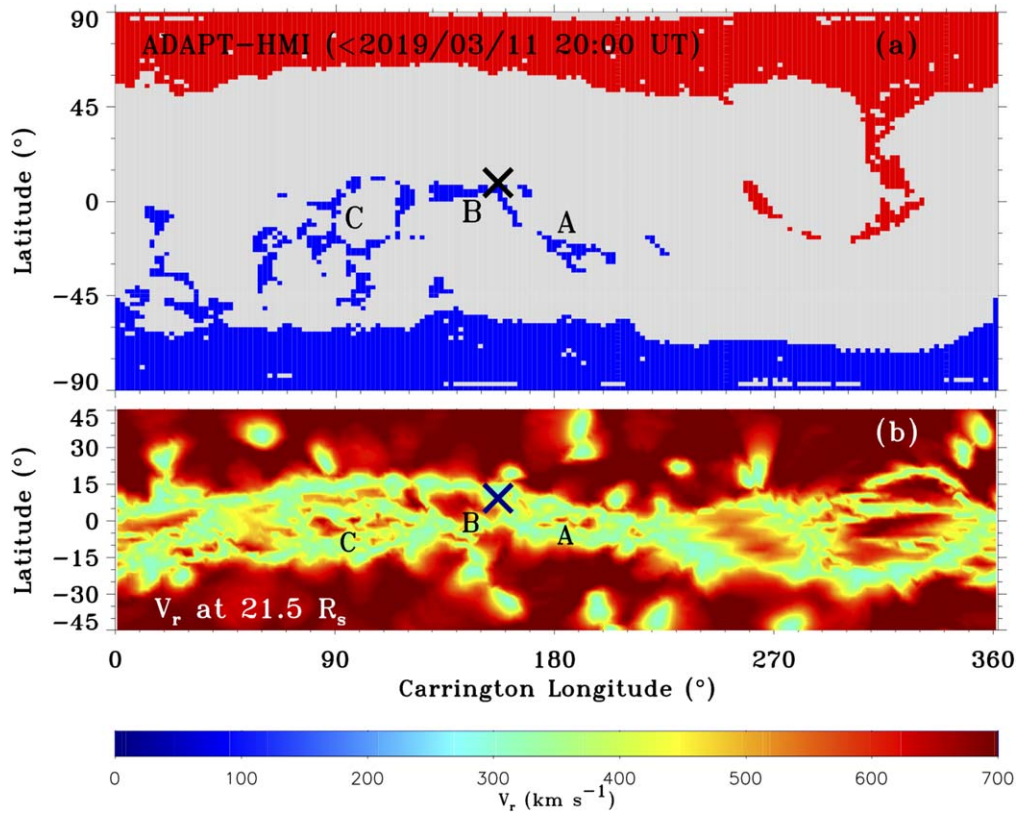
15

Figure 12. (a) Coronal hole map obtained from the ADAPT-WSA model using as input the synoptic SDO/HMI magnetograms collected during CR 2214 (last magnetogram used dates from 2019 March 11 at 20:00 UT). (b) Velocity map at 21.5 $R_\odot$ obtained by the WSA and used as input for the ENLIL code. The cross indicates the direction of the nose of the SBO-CME as represented by GCS applied at helioradii above 10 $R_\odot$. Letters A, B, and C indicate the CHs that are the origin of the high-speed streams described in Section 4.1.

Figure 13 shows a series of snapshots obtained from the ADAPT-WSA-ENLIL-Cone simulation at different times during the propagation of the ICME in IP space. The black arrow in Figure 13(a) indicates the central direction of the injected CME, and the black contours in Figures 13(b)–(f) identify the injected structure as it propagates in the IP medium. Figure 13(a) corresponds to an initial time when the input pulse was still crossing the ENLIL inner boundary at 21.5 $R_\odot$. High-speed streams identified with the letters A, B, and C correspond to those that can be associated with the speed patches A, B, and C in Figure 12(b). Figure 13(b) corresponds to the time when the field line connected to PSP intercepted the western edge of the ICME. As the ICME advances (Figures 13(c)–(d)), the intercept moves from the western flank closer to the nose of the ICME. Figure 13(e) shows a time just prior to the arrival of the ICME at PSP. ENLIL predicts that, using 1 hr resolution results, PSP intercepted the ICME on 2019 March 15 at 11:00 UT. This is just ∼1 hr earlier than the actual observation of the ICME leading edge by PSP at 12:14 UT. Both the ENLIL and GCS models (Figure 8) agree that PSP intercepted the western flank of the ICME, although the ICME structures differ due to the model assumptions. Figure 13(f) corresponds to a time when the ICME was already beyond PSP and the spacecraft was then observing the solar wind originating in CH A; though because of the limitations of the cone model, the near-radial orientation of the ICME leg in Figure 8 is not reproduced in Figure 13. Note that the ICME was distorted during propagation through the structured solar wind, especially by fast streams A and B. Such distortion is not taken into account in the GCS model in Figure 8 but may have occurred.

4.3. PSP Magnetic Field Connection and Energetic Particle Event

Using the type of simulations described in Section 4.2, it is possible to estimate when PSP established magnetic connection with the compressed plasma formed upstream of the ICME. We have followed the same procedure as Bain et al. (2016) to determine whether PSP established magnetic connection with an enhanced solar wind speed region in front of the ICME. For this purpose, two ENLIL simulations were performed, one with just the background ambient solar wind and another including the ICME. We then evaluated the solar wind speed measured along the magnetic field line passing by PSP in the case where only the background ambient medium was considered and compared it with the solar wind speed measured along the corresponding field line in the simulation when the ICME was included. The first point on this field line where the solar wind speed increases above the ambient value corresponds to the location where the compressed region in front of the ICME establishes connection to PSP, often termed the "Connecting with the OBserving" point or "cobpoint" after Heras et al. (1995).

Figures 14(a) and (b) show the coordinates of this point, in particular its heliocentric radial distance $R_{\rm COB}$ and its longitude $\phi_{\rm COB}$ in the HEEQ coordinate system, as the cobpoint moved outward from the Sun together with the ICME. The horizontal thin lines in Figures 14(a) and (b) indicate the heliocentric radial distance of PSP ($R = 0.547$ au) and the HEEQ longitude of PSP ($-161°$ or equivalently, $199°$), respectively, at the time of the shocks' arrival. Figure 14(c) shows the factor by which the solar wind speed at the cobpoint increases with respect to
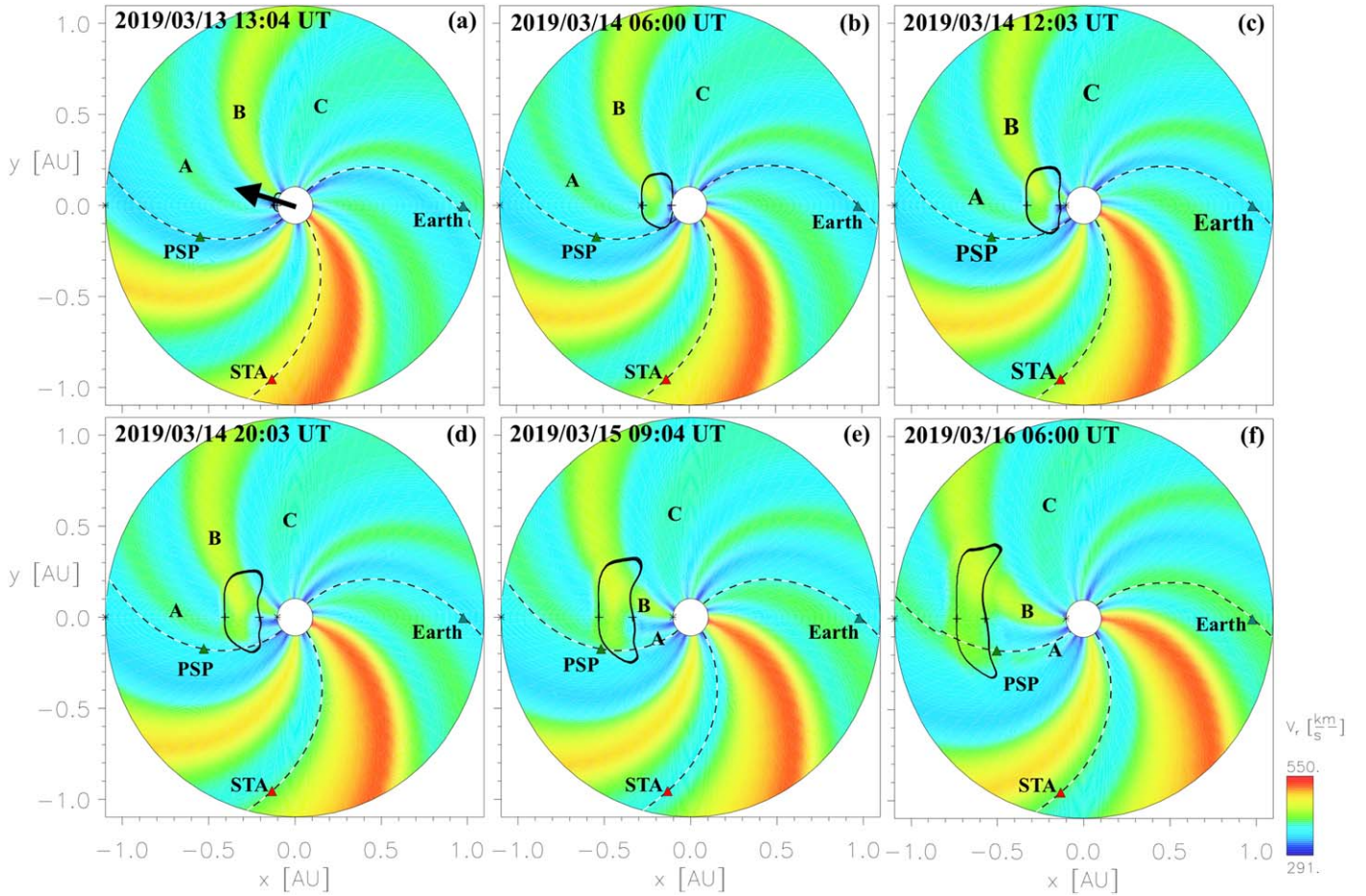
Figure 13. Solar wind speed contours obtained from the ENLIL simulation at different times during the ICME propagation toward PSP. The black contour identifies the injected pulse as it deforms and propagates toward PSP. The dashed black-white lines indicate the magnetic field lines traced from the position of PSP, STA, and Earth toward the ENLIL inner boundary using the simulated magnetic field vector. The letters A, B, and C identify the high-speed streams originating at the speed patches A, B, and C indicated in Figure 12(b), respectively.

the ambient simulation. Magnetic connection was established on 2019 March 14 at 5:00 UT as indicated by the vertical dashed purple line in Figure 14. During the time interval indicated by dotted graphs in the four top panels (09:00 UT to 19:00 UT on 2019 March 14), the portion of the ICME intercepted by the PSP field line was moving through background solar wind with approximately the same speed as the ICME, and hence no speed increase was generated, implying that PSP lost momentary connection with the shock. As the ICME propagated further outward, the PSP cobpoint moved closer to more central positions of the ICME (Figure 13(e)) where the speed increase was more pronounced (Figure 14(c)). The simulated cobpoint arrived at PSP at ∼10:00 UT. This is around one hour later than the actual arrival time of the shocks at PSP, and 2.25 hr earlier than the actual arrival time of the ICME leading edge (Figure 2). The resolution used in the ENLIL simulations does not allow for the detection of the two shocks actually observed by PSP, but the simulations do approximate the effects that the approaching ICME might have produced on the ambient medium.

Figure 14(d) shows an estimate of the speed of the cobpoint measured by comparing the cobpoint location at two consecutive times. It is interesting to compare the evolution of the cobpoint speed (Figure 14(d)) and the speed jump at the cobpoint (Figure 14(c)) with the time profile of the ∼30–500 keV ion intensities shown in Figure 14(e). Figure 14 suggests that particle

intensities initially increased around the time when PSP established magnetic connection with the compression region in front of the ICME, consistent with a shock driven by the ICME being the site of particle acceleration. There is then a slight intensity decrease that may be related to the temporary loss of connection to the shock (indicated by the dotted lines in Figures 14(a)–(d)). The increase in the speed jump before the arrival of the shock may then be associated with the further increase in particle intensities, though the ENLIL simulation does not reproduce the actual speed jumps observed at the shocks (Figure 4). The ∼20 minute interval between peak particle intensity and the shocks (Figure 2(n)) might indicate a dynamic evolution of the shock parameters or that PSP established magnetic connection with a stronger remote portion of the shocks prior to their actual arrival at PSP.

Figures 14(f)–(h) show the particle intensities as a function of energy detected by the EPI-Lo IonToF system. EPI-Lo consists of eight wedges with 10 apertures in each wedge (see Figures 1 and 2 in Hill et al. 2017). As ions enter the apertures of EPI-Lo, they generate secondary electrons as they pass through the start foils. The ions then continue and strike a solid state detector where they generate secondary electrons for the stop signal (see Figure 3 in Hill et al. 2017). The difference between the start and stop times provides an estimation of the ToF of the incident ions. IS⊙IS team assigns an energy to these ToF data products under the assumption that particle
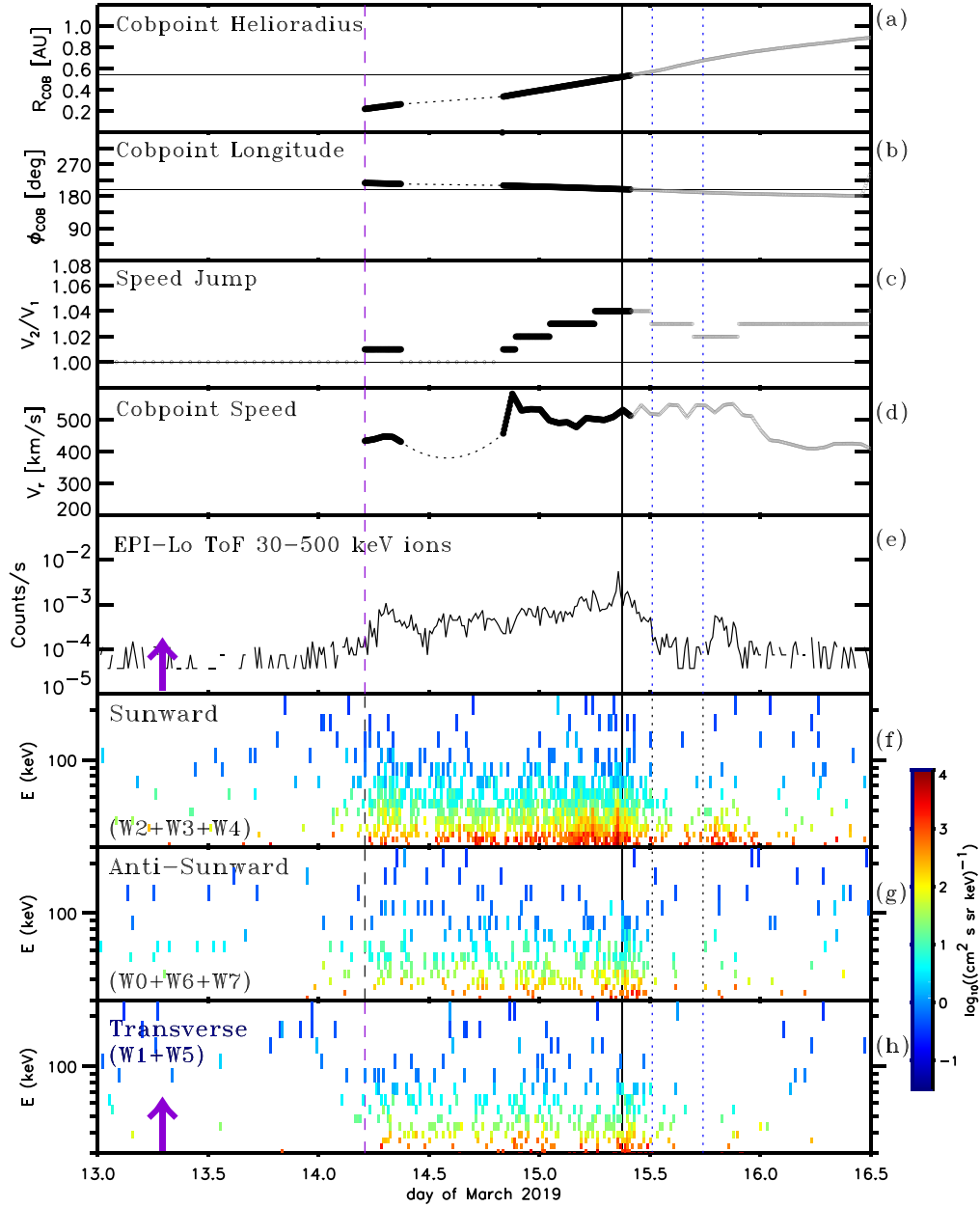
Figure 14. (a) Heliocentric radial distance of the PSP cobpoint, (b) HEEQ longitude of the PSP cobpoint, (c) speed jump ratio measured at the PSP cobpoint when comparing ENLIL background simulation with the simulation including the ICME, (d) speed of the cobpoint, (e) ion intensities at energies ∼30–500 keV as measured by the IonToF system of EPI-Lo, (f) ion intensities measured by the IonToF system in the Sun-facing wedges of EPI-Lo, (g) ion intensities measured by the IonToF system in the wedges of EPI-Lo pointing opposite to the Sun, and (h) ion intensities measured by the IonToF system in the transverse wedges. The vertical solid lines indicate the passage of the two shocks (not resolvable at this timescale), and the vertical dotted lines indicate the boundaries of the ICME. The vertical purple dashed line indicates the time when magnetic connection between PSP and the compression region formed in front of the ICME was first established. The purple vertical arrows indicate the time when the parent SBO-CME accelerated (see Section 3).

intensities are dominated by protons, an assumption that usually, though not always, is well justified (Desai et al. 2020; Giacalone et al. 2020). In Figure 14(f), we have added the IonToF particle fluxes measured through all of the apertures of the EPI-Lo wedges looking in the sunward direction (W2, W3, and W4), under the assumption that all apertures have similar geometric factors and energy windows. Similarly, Figure 14(g) shows the particle fluxes obtained by summing over the wedges looking in the anti-sunward direction (W0, W7, and W6). Finally, Figure 14(h) considers only the two wedges looking in the transverse direction (W1 and W5). In the spacecraft frame

of reference, the energetic particle event was clearly anisotropic throughout the time interval prior to the arrival of the shocks, with particle intensities dominated by the sunward-looking wedges. Only after the passage of the shocks were the intensities measured in the anti-sunward and transverse wedges populated, suggesting a more isotropic distribution. This anisotropy analysis is preliminary. In particular, the Compton-Getting effect (e.g., Ipavich 1974) has not been taken into account, mainly because there have been insufficient SEP events observed so far in the PSP mission to allow for the response of the complex EPI-Lo instrument, including the
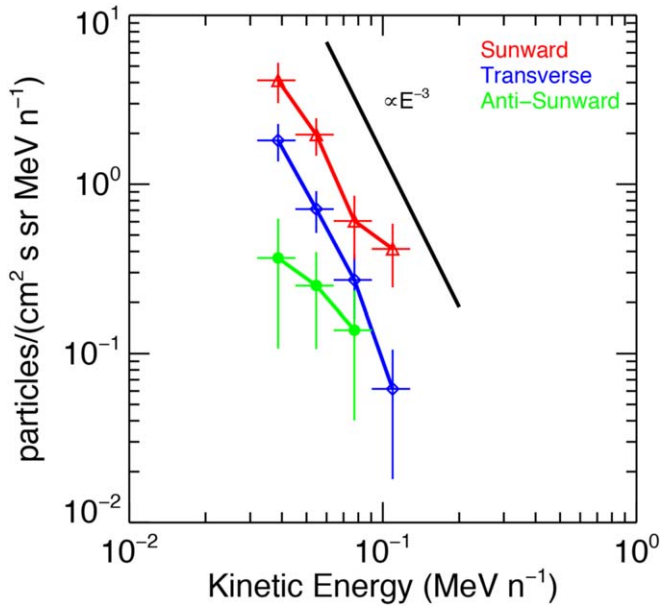
Figure 15. Differential energy spectra of He ions averaged over the time interval 2019 March 13 12:00 UT–2019 March 15 18:00 UT. The three spectra are averaged over the EPI-Lo apertures looking in the sunward (red), transverse (blue), and anti-sunward (green) directions as described by Desai et al. (2020). The solid line shows a differential intensity spectrum of the form $dJ/dE \propto E^{-3}$ for comparison with the three spectra.

efficiencies and energy ranges, to be completely determined. However, the preferential detection of particles in the sunward-looking wedges before the arrival of the shocks suggests that particles were coming mostly from the direction of the approaching traveling shocks, and that they were observed by PSP when the spacecraft established magnetic connection to the shocks. The evolution of the particle intensity–time profile, increasing at the time of connection, peaking close to the arrival of the shocks, and with fluctuations resulting from changing connections to different portions of the shocks, dynamic evolution of the shocks properties, or even momentary loss of connection, agrees with a moving source that is injecting particles at a rate that is proportional to the speed jump at the cobpoint (e.g., Lario et al. 1998).

Apart from the IonToF data product, EPI-Lo also provides triple coincidence data that allow for computation of the ion mass with low background but poor counting statistics. Thus, in small events, it is necessary to sum observations over long intervals and several look directions and energies. Figure 15 shows the He differential energy spectra averaged over the time interval 2019 March 13 12:00 UT–2019 March 15 18:00 UT that essentially encompasses the whole SEP event. The three displayed spectra are obtained from the triple coincidence data in the sunward, transverse, and anti-sunward directions as defined in Desai et al. (2020). Figure 15 illustrates the anisotropic character of the event with a sunward to anti-sunward ~40 keV/n He event-averaged intensity ratio in the spacecraft frame of reference of about 1 to 16. Figures 14(f)–(g) and 15 show that the particle event was limited to energies $\lesssim 100$ keV/n and that the event-averaged He energy spectrum between 40 and 100 keV/n follows in a very good approximation a steep E^{-3} dependence. If this spectrum resulted from the quasi-linear diffusive shock acceleration (DSA) mechanism (e.g., Lee 1983), it would correspond to a shock compression ratio $r_n \sim 1.6$ that is larger than that estimated from the in situ measurements of the two shocks (Section 2.2).

	S (au)	$\langle B \rangle$ (nT)	$\langle N_p \rangle$ (cm^{-3})	$\langle T_p \rangle$ (K)
This ICME	0.054	30.4	30.4	3.0×10^4
Forsyth et al. (2006)	0.225	22.7	26.0	7.3×10^4
Liu et al. (2005)	0.143	17.1	25.0	4.3×10^4

However, event-averaged intensities include particles accelerated at different stages of the shock propagation, and they necessarily involve particles accelerated at different times and from different regions of the shock (e.g., Lario et al. 1998). Additionally, the presence of two shocks, with possible processes of shock dissipation and reformation, might have led to complex processes of particle acceleration that are not described by simple DSA. Therefore, the inference of a shock compression ratio from an event-averaged spectrum and assuming a certain shock acceleration model has no real meaning, apart from the fact that such a steep spectrum implies an inefficient accelerator of particles at high energies.

5. Discussion

We first revisit the properties of the ICME. The flux-rope-like characteristics of the magnetic field inside the ICME observed in situ by PSP between 12:14 UT and 17:45 UT on 2019 March 15 were similar to those found in ICMEs that include "MCs" observed at 1 au and also in the inner heliosphere by the Helios spacecraft (e.g., Burlaga et al. 1982; Klein & Burlaga 1982; Kilpua et al. 2017, and references therein). Data shown in Figure 1 allow us to compute the mean magnetic field magnitude $\langle B \rangle$, the mean density $\langle N_p \rangle$, and the mean temperature $\langle T_p \rangle$ measured during the passage of the ICME at PSP, as well as the radial size S of the ICME computed as the measured mean speed times the ICME duration. The first row of Table 2 lists these measured parameters. Averaged radial dependences of ICME parameters deduced from Helios observations (e.g., Table 1 and Figure 6 in Forsyth et al. 2006) or combining Helios with data from spacecraft beyond 1 au (e.g., Liu et al. 2005) allow us to compute the expected parameters for an observer at 0.547 au as listed in the second and third rows of Table 2. The radial size of this ICME at PSP departs most strongly from the expected average values. This may be a selection bias since its short duration (5.52 hr) most likely would not have met the selection criteria for events in previous studies. In addition, it appears that PSP grazed the edge of the leg of the ICME (Figure 8), so S may not be a good estimate of the diameter of the flux rope. Indeed, model fits (Table 1) suggest that this ICME contained an unusually small cross-sectional flux rope (with a radius of only 0.0129 au as inferred by the EC model), and the much larger value of S is consistent with an encounter along the axial direction rather than transverse to the flux rope. The larger-than-expected mean density and magnetic field intensity may be a consequence of the pressure exerted by the trailing HSS and the resulting compression of the ICME, or also due to event-to-event variations. Solar wind deflections evident in V_T (Figure 2(b)), the sudden increase in $P_{\rm dyn}$ (Figure 2(k)) at the trailing edge of the ICME, and the flat profiles of B and V_R

throughout the transit of the ICME (Figures 1(a) and (f)) are evidence of the compression effects of the trailing HSS. This compression, however, did not translate into an elevated averaged value of T_p, with the caveat that different instrumentation and analysis methods can also impact comparisons of T_p, in addition to event-to-event variations. The observed low mean value of T_p may be a consequence of the streamer blowout origin of this ICME, since most likely SBO-CMEs involve some magnetic reconnection mechanism at higher altitudes, resulting in a smaller amount of magnetic energy being available than for CMEs near active regions (Vourlidas & Webb 2018), leading to less heating of the CME plasma.

We also suggest that interactions with the structured ambient solar wind, in particular with the HSS, may have influenced the propagation of the ICME to PSP. Whereas multi-spacecraft coronagraph images suggest an estimated speed of just $311 \, \mathrm{km \, s^{-1}}$ at $\sim 10–15 \, R_\odot$ for the leading edge of the SBO-CME, the transit time from the Sun (at 04:54 UT on 2019 March 13) to its arrival at PSP (at 12:14 UT on 2019 March 15) translates to an average transit speed of $\sim 410 \, \mathrm{km \, s^{-1}}$. Since PSP actually intercepted the flank of the ICME rather than near its nose (Figure 8), this implies that the acceleration of the leading edge of the ICME was larger than suggested by this transit speed. The initial speed of the SBO-CME inferred from coronagraph observations was relatively low compared to the solar wind and Alfvén speeds computed by the MAST model (Figure 10), indicating that the probability of driving a shock in the solar corona was relatively low. We suggest that the effect of the HSS on the ICME at larger heliocentric distances increased the transit speed of the ICME and the probability of it driving a shock when arriving at PSP.

We now discuss the origin of the two-shock structure observed by PSP before the arrival of the ICME (Figure 4). Figure 13(e) suggests that the plasma compression associated with the CIR formed upstream of fast stream A was in the vicinity of PSP at the time of the arrival of the shocks. Since the leading edge of a CIR can steepen into a forward shock, it is possible that the first shock was associated with the CIR that formed in front of the fast stream A, and the second was driven by the ICME. However, the rarity of CIR shocks in the inner heliosphere (e.g., Richter et al. 1985; Jian et al. 2008), the small temporal separation of the two shocks, and their similar orientations argue against the possibility that one of the shocks is a CIR shock. Another possibility is that the two shocks resulted from ICMEs associated with two consecutive solar eruptions, and the shock ahead of the second ICME had overtaken the leading ICME. However, the simple, well-formed ICME at PSP argues against the presence of ICME material from multiple eruptions unless only the flank of the shock associated with the second ICME, and not the ICME itself, encountered PSP. But again, the similar shock characteristics tend to argue against the shocks being of different origins. For these reasons, we suggest that the two-shock structure observed in Figure 4 was a response to the local conditions (including distortion of the ICME by the HSS) that caused the transition between the upstream and downstream plasma to occur in two steps. Consecutive shocks separated in time from seconds to 30 minutes have been previously observed at 1 au (e.g., Russell et al. 2009) and even at 0.47 au (in this case, separated by only 6 s; see Figure 9 in Lai et al. 2012). These authors suggested that these shocks could merge as they move outward and then constitute a single shock

at larger heliocentric distances. The two-step transition at the shocks may have been a response to the interaction between the ICME and the trailing HSS impacting the dynamics of the ICME.

The ADAPT-WSA-ENLIL-Cone simulation corroborates that (1) the ICME interacted with the structured solar wind and (2) PSP intercepted the western flank of the ICME as predicted from (a) the reconstruction of the 3D morphology of the MC, (b) the self-similar expansion of the GCS flux-rope structure (Figure 8), and (c) the imbalance in the BDEs during the ICME passage (Figure 2). However, several approximations are made in the ADAPT-WSA-ENLIL-Cone simulations. For instance, modeling of the ambient solar wind in the direction of PSP required using old magnetogram data because PSP was located on the opposite side of the Sun from Earth. While the ADAPT model attempts to compensate for this by incorporating established magnetic flux transport processes when new observations are not available, it cannot account for the emergence of new flux on the solar far side. This problem can greatly impact solar wind solutions on the far side or even globally. The variations seen in the CH structure between CR 2214 and CR 2215 (Figure 10) clearly imply evolution in the coronal field, and thus the inferred large-scale CH structure at the time of the CME is approximate. Moreover, ENLIL does not simulate the ICME as a magnetic ejecta; the ICME is introduced just as a high-pressure region to emulate the observed ICME-related solar wind disturbances. Therefore, any deformation of the initial ICME structure depicted in Figure 13 is just an indication of the possible effects produced by the structured solar wind.

Despite all of these uncertainties, ENLIL simulations still give an idea of the large-scale magnetic connection between PSP and a possible shock driven by the ICME. It is interesting that, in general, the evolution of the speed jump at the cobpoint is consistent with the particle intensity–time profile, at least throughout the time interval prior to the shock arrival. This will be addressed further in a future study using the evolution of the speed increase measured at the PSP cobpoint to predict the evolution of the particle intensities measured by PSP (e.g., Luhmann et al. 2017). Both the modest speed jump inferred at the cobpoint (Figure 14(c)), as well as the shock parameters inferred from in situ measurements (Figure 4), suggest that the shocks were weak and inefficient at accelerating particles consistent with observations showing few particles above $\sim 100 \, \mathrm{keV/n}$. The initial propagation of the SBO-CME through the streamer belt and the presence of CIR particles, at least at 1 au (Figure 9(h)), might suggest the presence of a seed population for the processes of particle acceleration at shocks (Kahler & Vourlidas 2005). However, multiple factors play a role in the acceleration of particles at shocks, and remote-sensing observations can provide only general estimates of shock properties in the corona (e.g., Lario et al. 2017). PSP established magnetic connection with the western flank of the solar wind disturbance ahead of the ICME, when this structure was already in IP space ($R_{\mathrm{COB}} \sim 0.2 \, \mathrm{au}$). The anti-sunward arrival of particles at PSP at this time and for almost two days before the HSS (Figures 14(e)–(h) and 15) is consistent with the continuous injection of particles. The trailing HSS increased the speed of the SBO-CME so that it was able to generate a pair of shocks that resulted in an energetic particle event, although this was limited to low ($\lesssim 100 \, \mathrm{keV/n}$) energies.

6. Summary and Final Remarks

An ICME observed by PSP on 2019 March 15 when on the far side of the Sun from Earth was associated with a slow SBO-CME on the Sun as observed by coronagraphs on both STA and SOHO. The in situ properties of the ICME resemble those of an MC. Remote-sensing observations from multiple spacecraft allowed us to reconstruct the orientation and large-scale structure of the SBO-CME that, assuming self-similar expansion, intercepted PSP along its western leg. Consistent with this, reconstruction of the MC magnetic field topology indicates that the MC axis was approximately in a radial direction. An HSS compressing the trailing edge of the ICME may also have distorted, compressed, and accelerated the ICME, possibly contributing to the production of a pair of closely spaced shocks upstream of the ICME. These weak shocks were accompanied by a low-energy (<100 keV/n) ion enhancement that appears, according to ENLIL modeling, to have commenced when magnetic connection was established between PSP and the compression region ahead of the ICME. However, the shocks were extremely weak, and the energetic particle event was just a low-energy ($\lesssim100$ keV/n) phenomenon. Thus, this study demonstrates that, although SBO-CMEs are usually slow close to the Sun, subsequent evolution in IP space may lead them to drive shocks that can accelerate particles in the inner heliosphere. This ICME was embedded in a CIR. Around 9% of CIRs at 1 au have an embedded ICME, and they may be important drivers of geomagnetic activity (e.g., Jian et al. 2019). Thus, this study helps to understand the solar origins of such events and their evolution in the inner heliosphere.

In conclusion, the present study has shown how a compilation of data from multiple spacecraft and a variety of instruments, including remote-sensing and in situ observations, can be used to construct a scenario for a small transient event observed by PSP. However, there are uncertainties in the interpretation arising from the spacecraft configuration, the small size of the event, and its solar origin in the low corona. Small energetic particle events associated with modest transients such as those discussed here may contribute to the seed population for SEP events accelerated by shocks propagating through the inner heliosphere. Both PSP and Solar Orbiter operating in the inner heliosphere, with unprecedented instrument sensitivity, will allow for studies of such events and thus determine the contribution of these small solar eruptions to the energetic particle population in the inner heliosphere.

Appendix

Figures A1 and A2 are snapshots of the animations available in the online version of the journal. They show the SBO-CME origin of the ICME observed in situ by PSP on 2019 March 15 as seen by STA/COR1 and STA/COR2.
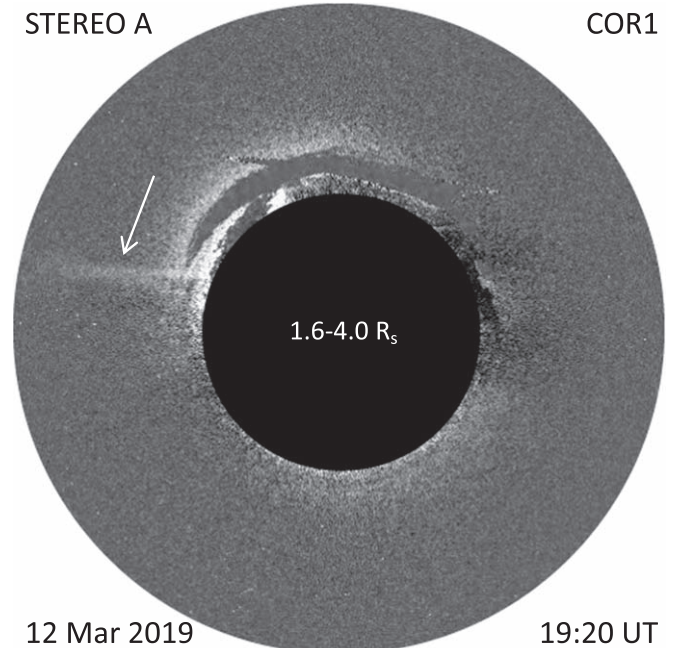

Figure A1. STEREO-A/COR1 white-light image taken on 2019 March 12 at 19:20 UT. The image has been processed with a wide and a narrow Gaussian filter in time as described in the text following the method of Alzate et al. (2020). The FOV, as shown, spans a distance from 1.6 to 4.0 $R_{\odot}$. The arrow points to coronal material that propagates across the FOV of COR1 following the brightening of the streamer belt over the east limb of the Sun between 75° and 90° counterclockwise from north. A time series of observations shows the coronal material propagating beginning on 2019 March 12 until approximately 05:00 UT on 2019 March 13 when the material appears to disconnect.

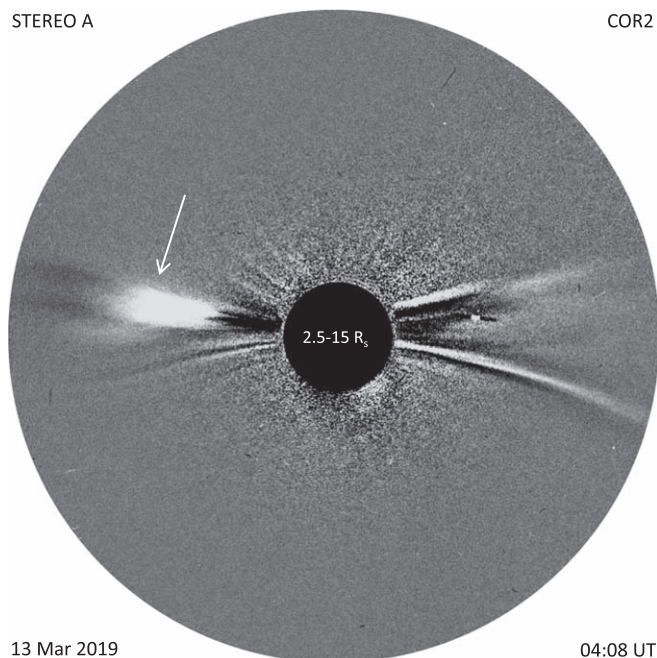(An animation of this figure is available.)

Figure A2. STEREO-A/COR2 white-light image taken on 2019 March 13 at 04:08 UT. The image has been processed using the same method as for COR1. The FOV, as shown, spans a distance from 2.5 to 15 $R_\odot$. The arrow points to the SBO-CME over the east limb of the Sun between 75° and 90° counterclockwise from north. A time series of observations shows the expansion and propagation across the FOV of COR2 of the coronal material from COR1, that entered the FOV of COR2 approximately midday on 2019 March 12. As it propagates, it undergoes a small acceleration at approximately 01:00 UT on 2019 March 13 and later at approximately 05:00 UT when more outflowing material can be seen entering the FOV.

(An animation of this figure is available.)

ORCID iDs

D. Lario ● https://orcid.org/0000-0002-3176-8704
L. Balmaceda ● https://orcid.org/0000-0003-1162-5498
N. Alzate ● https://orcid.org/0000-0001-5207-9628
I. G. Richardson ● https://orcid.org/0000-0002-3855-3634
R. C. Allen ● https://orcid.org/0000-0003-2079-5683
T. Nieves-Chinchilla ● https://orcid.org/0000-0003-0565-4890
N. Lugaz ● https://orcid.org/0000-0002-1890-6156
L. K. Jian ● https://orcid.org/0000-0002-6849-5527
M. I. Desai ● https://orcid.org/0000-0002-7318-6008
P. L. Whittlesey ● https://orcid.org/0000-0002-7287-5098
J. G. Luhmann ● https://orcid.org/0000-0003-0626-9353

References

Acuña, M. H., Curtis, D., Scheifele, J. L., et al. 2008, SSRv, 136, 203
Alzate, N., Morgan, H., Viall, N., & Vourlidas, A. 2020, ApJ, submitted
Arge, C. N., Henney, C. J., Koller, J., et al. 2010, in AIP Conf Proc 1216, Twelfth Int. Solar Wind Conf., ed. M. Maksimovic et al. (Melville, NY: AIP), 343
Arge, C. N., Luhmann, J. G., Odstrcil, D., et al. 2004, JASTP, 66, 1295
Bain, H. M., Mays, M. L., Luhmann, J. G., et al. 2016, ApJ, 825, 1
Bale, S. D., Goetz, K., Harvey, P. R., et al. 2016, SSRv, 204, 49
Brueckner, G. E., Howard, R. A., Koomen, M. J., et al. 1995, SoPh, 162, 357
Burlaga, L. F., Klein, L., Sheeley, N. R., et al. 1982, GeoRL, 9, 1317
Carcaboso, F., Gomez-Herrero, R., Espinosa-Lara, F., et al. 2020, A&A, 635, A79
Cartwright, M. L., & Moldwin, M. B. 2008, JGRA, 113, A09105
Cartwright, M. L., & Moldwin, M. B. 2010a, JGRA, 115, A10110
Cartwright, M. L., & Moldwin, M. B. 2010b, JGRA, 115, A08102
Case, A. W., Kasper, J. C., Stevens, M. L., et al. 2020, ApJS, 246, 43
Case, A. W., Spence, H. E., Owens, M. J., et al. 2008, GeoRL, 35, L15105
DeForest, C. E., Howard, T. A., & McComas, D. J. 2013, ApJ, 769, 43
Desai, M. I., Mitchell, D. G., Szalay, J. R., et al. 2020, ApJS, 246, 56
Feldman, W. C., Anderson, R. C., Bame, S. J., et al. 1983, JGR, 88, 9949
Forsyth, R. J., Bothmer, V., Cid, C., et al. 2006, SSRv, 123, 383
Galvin, A. B., Kistler, L. M., Popecki, M. A., et al. 2008, SSRv, 136, 437
Giacalone, J., Mitchell, D. G., Allen, R. C., et al. 2020, ApJS, 246, 29
Gold, R. E., Krimigis, S. M., Hawkins, S. E., et al. 1998, SSRv, 86, 541
Gonzàlez-Àlvarez, M. 2019, Analysis of Interplanetary Coronal Mass Ejections Observed by STEREO and MESSENGER, Bachelor's thesis, Universitat Politècnica de Catalunya, https://upcommons.upc.edu/handle/2117/168746
Gopalswamy, N., Lara, A., Lepping, R. P., et al. 2000, GeoRL, 27, 145
Gosling, J. T. 1990, in Physics of Magnetic Flux Ropes, ed. C. T. Russell, E. R. Priest, & L. C. Lee, Vol. 58 (Washington, DC: AGU), 343
Gulisano, A. M., Démoulin, P., Dasso, S., et al. 2010, A&A, 509, A39
Gulisano, A. M., Démoulin, P., Dasso, S., et al. 2012, A&A, 543, A107
He, W., Liu, Y. D., Hu, H., et al. 2018, ApJ, 860, 78
Heinemann, S. G., Temmer, M., Farrugia, C. J., et al. 2019, SoPh, 294, 121
Henney, C. J., Toussaint, W. A., White, S. M., et al. 2012, SpWea, 10, S02011
Heras, A. M., Sanahuja, B., Lario, D., et al. 1995, ApJ, 445, 497
Hickmann, K. S., Godinez, H. C., Henney, C. J., et al. 2015, SoPh, 290, 1105
Hidalgo, M. A., Cid, C., Vinas, A. F., et al. 2002, JGRA, 107, 1002
Hill, M. E., Mitchell, D. G., Andrews, G. B., et al. 2017, JGRA, 122, 1513
Howard, R. A., Moses, J. D., Vourlidas, A., et al. 2008, SSRv, 136, 67
Illing, R. M. E., & Hundhausen, A. J. 1984, BAAS, 16, 454
Ipavich, F. M. 1974, GeoRL, 1, 149
Janvier, M., Winslow, R. M., Good, S., et al. 2019, JGRA, 124, 812
Jian, L. K., Luhmann, J. G., Russell, C. T., et al. 2019, SoPh, 294, 31
Jian, L. K., Russell, C. T., Luhmann, J. G., et al. 2008, SoPh, 249, 85
Jian, L. K., Russell, C. T., Luhmann, J. G., et al. 2018, ApJ, 855, 114
Kahler, S. W., Crooker, N. U., & Gosling, J. T. 1999, JGR, 104, 9911
Kahler, S. W., & Vourlidas, A. 2005, JGRA, 110, A12S01
Kasper, J. C., Abiad, R., Austin, G., et al. 2016, SSRv, 204, 131
Kay, C., & Opher, M. 2015, ApJL, 811, L36
Kilpua, E., Koskinen, H. E. J., & Pulkkinen, T. I. 2017, LRSP, 14, 5
Klein, L. W., & Burlaga, L. F. 1982, JGR, 87, 613
Korreck, K. E., Szabo, A., Chinchilla, T. N., et al. 2020, ApJS, 246, 69
Koval, A., & Szabo, A. 2008, JGRA, 113, A10110
Koval, A., & Szabo, A. 2010, JGRA, 115, A12105
Lai, H. R., Russell, C. T., Jian, L. K., et al. 2012, SoPh, 278, 421
Lario, D., Hu, Q., Ho, G. C., et al. 2005, in Solar Wind 11/SOHO 16, Connecting Sun and Heliosphere, ed. B. Fleck, T. H. Zurbuchen, & H. Lacoste (Paris: ESA), 81
Lario, D., Kwon, R.-Y., Riley, P., & Raouafi, N. E. 2017, ApJ, 847, 103
Lario, D., Sanahuja, B., & Heras, A. M. 1998, ApJ, 509, 415
Lee, M. A. 1983, JGR, 88, 6109
Lemen, J. R., Title, A. M., Akin, D. J., et al. 2012, SoPh, 275, 17
Liewer, P., Panasenco, O., Vourlidas, A., et al. 2015, SoPh, 290, 3343
Linker, J. A., Caplan, R. M., Downs, C., et al. 2017, ApJ, 848, 70
Lionello, R., Linker, J. A., & Mikić, Z. 2009, ApJ, 690, 902
Liu, Y., Richardson, J. D., & Belcher, J. W. 2005, P&SS, 53, 3
Liu, Y., Shen, F., & Yang, Y. 2019, ApJ, 887, 150
Liu, Y. D., Hu, H., Wang, C., et al. 2016, ApJS, 222, 23
Luhmann, J. G., Mays, M. L., Odstrcil, D., et al. 2017, SpWea, 15, 934
Lynch, B. J., Li, Y., Thernisien, A. F. R., et al. 2010, JGRA, 115, A07106
Lynch, B. J., Masson, S., Li, Y., et al. 2016, JGRA, 121, 10,677
Mäkelä, P., Gopalswamy, N., Xie, H., et al. 2013, SoPh, 284, 59
Mason, G. M., & Sanderson, T. R. 1999, SSRv, 89, 77
Mays, M. L., Taktakishvili, A., Pulkkinen, A., et al. 2015, SoPh, 290, 1775
McComas, D. J., Alexander, N., Angold, N., et al. 2016, SSRv, 204, 187
McComas, D. J., Bame, S. J., Barker, P., et al. 1998, SSRv, 86, 563
Mitchell, D. G., Giacalone, J., Allen, R. C., et al. 2020, ApJS, 246, 59
Morgan, H. 2015, ApJS, 219, 23
Morgan, H., Byrne, J. P., & Habbal, S. R. 2012, ApJ, 752, 144
Müller-Mellin, R., Böttcher, S., Falenski, J., et al. 2008, SSRv, 136, 363
Nieves-Chinchilla, T., Colaninno, R., Vourlidas, A., et al. 2012, JGRA, 117, A06106
Nieves-Chinchilla, T., Linton, M. G., Hidalgo, M. A., et al. 2016, ApJ, 823, 27
Nieves-Chinchilla, T., Linton, M. G., Hidalgo, M. A., et al. 2018a, ApJ, 861, 139
Nieves-Chinchilla, T., Szabo, A., Korreck, K. E., et al. 2020, ApJS, 246, 63
Nieves-Chinchilla, T., Vourlidas, A., Raymond, J. C., et al. 2018b, SoPh, 293, 25

Nitta, N. V., & Mulligan, T. 2017, SoPh, 292, 125
Odstrcil, D., Mays, M. L., Hess, P., et al. 2020, ApJS, 246, 73
Odstrcil, D., Riley, P., & Zhao, X. P. 2004, JGRA, 109, A02116
Phillips, J. L., Gosling, J. T., McComas, D. J., et al. 1992, in Solar Wind Seven: Proceedings of the 3rd Cospar Colloquium, ed. E. Marsch & R. Schwenn, Vol. 3 (Oxford: Pergamon), 651
Pilipp, W. G., Miggenrieder, H., Montgomery, M. D., et al. 1987, JGR, 92, 1093
Pizzo, V. J., de Koning, C., Cash, M., et al. 2015, SpWea, 13, 676
Pulupa, M., & Bale, S. D. 2008, ApJ, 676, 1330
Richardson, I. G. 2018, LRSP, 15, 1
Richter, A. K., Hsieh, K. C., Luttrell, A. H., et al. 1985, in Collisionless Shocks in the Heliosphere: Reviews of Current Research, ed. B. T. Tsurutani & R. G. Stone, Vol. 35 (Washington, DC: AGU), 33
Riley, P., Linker, J. A., Lionello, R., et al. 2012, JASTP, 83, 1
Riley, P., Lionello, R., Linker, J. A., et al. 2011, SoPh, 274, 361
Rouillard, A. P., Savani, N. P., Davies, J. A., et al. 2009, SoPh, 256, 307
Russell, C. T., Jian, L. K., Blanco Cano, X., et al. 2009, GeoRL, 36, L02103
Schatten, K. H. 1971, CosEl, 2, 232
Schatten, K. H., Wilcox, J. M., & Ness, N. F. 1969, SoPh, 6, 442
Scherrer, P. H., Schou, J., Bush, R. I., et al. 2012, SoPh, 275, 207
Schwenn, R., Mohlhauser, K. H., & Rosenbauer, H. 1981, in Solar Wind 4, ed. H. Rosenbauer (Garching: Max-Planck-Institute für Aeronomie), 118
Schwenn, R., Montgomery, M. D., Rosenbauer, H., et al. 1978, JGR, 83, 1011
Sheeley, N. R., Howard, R. A., Koomen, M. J., et al. 1982, SSRv, 33, 219
Siscoe, G., & Odstrcil, D. 2008, JGRA, 113, A00B07
Smith, C. W., L'Heureux, J., Ness, N. F., et al. 1998, SSRv, 86, 613
St. Cyr, O. C., Plunkett, S. P., Michels, D. J., et al. 2000, JGR, 105, 18169
Thernisien, A. 2011, ApJS, 194, 33
Thernisien, A., Vourlidas, A., & Howard, R. A. 2009, SoPh, 256, 111
Thernisien, A. F. R., Howard, R. A., & Vourlidas, A. 2006, ApJ, 652, 763
Volkmer, P. M., & Neubauer, F. M. 1985, AnGeo, 3, 1
Vourlidas, A., & Webb, D. F. 2018, ApJ, 861, 103
Wallace, S., Arge, C. N., Pattichis, M., et al. 2019, SoPh, 294, 19
Webb, D. F., & Vourlidas, A. 2016, SoPh, 291, 3725
Whittlesey, P. L., Larson, D. E., Kasper, J. C., et al. 2020, ApJS, 246, 74
Wiedenbeck, M. E., Angold, N. G., Birdwell, B., et al. 2017, ICRC (Busan), 301, 16
Wuelser, J.-P., Lemen, J. R., Tarbell, T. D., et al. 2004, Proc. SPIE, 5171, 111
Zurbuchen, T. H., & Richardson, I. G. 2006, SSRv, 123, 31